Article

Cell

Endosome-ER Contacts Control Actin Nucleation and Retromer Function through VAP-Dependent Regulation of PI4P

Graphical Abstract

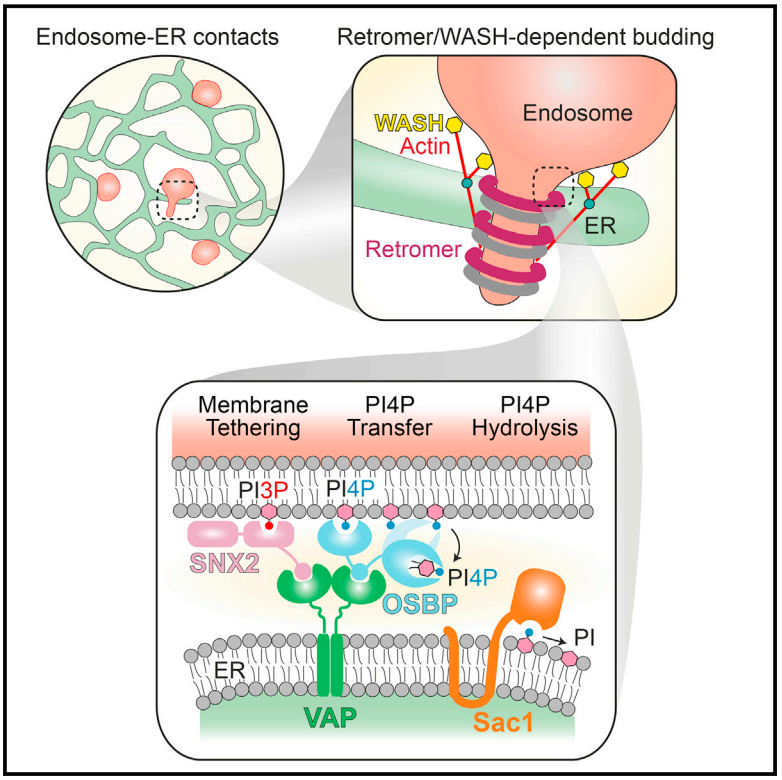

Authors

Rui Dong, Yasunori Saheki, Sharan Swarup, Louise Lucast, J. Wade Harper, Pietro De Camilli

Correspondence

pietro.decamilli@yale.edu

In Brief

Contacts between the membranes of two organelles influences vesicle budding through changes in lipid composition that affect actin dynamics.

Highlights

- An interaction between VAP and the retromer subunit SNX2 tethers the ER to endosomes
- Segregation of TGN proteins from endosomes is impaired in cells that lack VAP
- A PI4P pool regulated by OSBP accumulates on endosomes of VAP double KO cells
- WASH mediates potent actin nucleation from endosomes in cells lacking VAP or OSBP

Dong et al., 2016, Cell *166*, 408–423
July 14, 2016
http://dx.doi.org/10.1016/j.cell.2016.06.037

CellPress

Cell

Article

Endosome-ER Contacts Control Actin Nucleation and Retromer Function through VAP-Dependent Regulation of PI4P

Rui Dong,[1,2,3,5] Yasunori Saheki,[1,2,3,5,7] Sharan Swarup,[6] Louise Lucast,[1,2,3,5] J. Wade Harper,[6] and Pietro De Camilli[1,2,3,4,5,*]

[1]Department of Neuroscience, Yale University School of Medicine, New Haven, CT 06510, USA
[2]Department of Cell Biology, Yale University School of Medicine, New Haven, CT 06510, USA
[3]Howard Hughes Medical Institute, Yale University School of Medicine, New Haven, CT 06510, USA
[4]Kavli Institute for Neurosciences, Yale University School of Medicine, New Haven, CT 06510, USA
[5]Program in Cellular Neuroscience, Neurodegeneration and Repair, Yale University School of Medicine, New Haven, CT 06510, USA
[6]Department of Cell Biology, Harvard Medical School, Boston, MA 02115, USA
[7]Present address: Lee Kong Chian School of Medicine, Nanyang Technological University, Singapore 308232, Singapore
*Correspondence: pietro.decamilli@yale.edu
http://dx.doi.org/10.1016/j.cell.2016.06.037

SUMMARY

VAP (VAPA and VAPB) is an evolutionarily conserved endoplasmic reticulum (ER)-anchored protein that helps generate tethers between the ER and other membranes through which lipids are exchanged across adjacent bilayers. Here, we report that by regulating PI4P levels on endosomes, VAP affects WASH-dependent actin nucleation on these organelles and the function of the retromer, a protein coat responsible for endosome-to-Golgi traffic. VAP is recruited to retromer budding sites on endosomes via an interaction with the retromer SNX2 subunit. Cells lacking VAP accumulate high levels of PI4P, actin comets, and *trans*-Golgi proteins on endosomes. Such defects are mimicked by downregulation of OSBP, a VAP interactor and PI4P transporter that participates in VAP-dependent ER-endosomes tethers. These results reveal a role of PI4P in retromer-/WASH-dependent budding from endosomes. Collectively, our data show how the ER can control budding dynamics and association with the cytoskeleton of another membrane by direct contacts leading to bilayer lipid modifications.

INTRODUCTION

Trafficking of bilayer lipids within cells occurs both via vesicular transport and via lipid transfer proteins that directly carry them through the aqueous environment of the cytosol. At least a fraction of this direct transport occurs at contacts between membranes not leading to membrane fusion (Giordano et al., 2013; Holthuis and Menon, 2014; Lahiri et al., 2015; Levine and Loewen, 2006; Manford et al., 2012; Saheki et al., 2016; Stefan et al., 2011). Major players in direct lipid transport between the endoplasmic reticulum (ER) and other membranes are VAPA and VAPB (Scs2 and Scs22 in yeast), two homologous tail-anchored ER membrane proteins (Levine and Loewen, 2006). VAPs comprise an N-terminal MSP domain, which binds a variety of lipid transfer proteins containing the so-called FFAT motif (two phenylalanine in an acidic tract), a coiled-coil region responsible for homo/heterodimerization, and a C-terminal membrane anchor (Kaiser et al., 2005; Murphy and Levine, 2016). Several lipid transfer proteins that bind VAP through a FFAT motif can also bind other membranes in *trans*, thus tethering the ER to other membranes, while the lipid transfer module mediates lipid exchange (de Saint-Jean et al., 2011; Mesmin et al., 2013; Stefan et al., 2011).

Mutations in the MSP domain of VAPB (also called ALS8) that disrupt FFAT motif binding are responsible for a dominant form of amyotrophic lateral sclerosis (ALS) (Nishimura et al., 2004). It remains unclear whether the disease results from a dominant-negative effect of the mutant protein or from haploinsufficiency (Kabashi et al., 2013; Papiani et al., 2012; Teuling et al., 2007). Elucidating the impact of VAP loss-of-function may thus illuminate mechanisms of disease in addition to providing insights into fundamental aspects of lipid dynamics.

A major class of VAP interactors are members of the OSBP/ORP family (Osh proteins in yeast), which are defined by the presence of a lipid harboring module, the so-called OSBP-related domain (ORD). These proteins were originally thought to be dedicated to sterol transport (Dawson et al., 1989; Im et al., 2005; Olkkonen and Levine, 2004). However, recent studies suggested that they have heterogeneous lipid transport or countertransport functions, with a major shared property being the transport of PI4P (Chung et al., 2015; de Saint-Jean et al., 2011; Maeda et al., 2013; Mesmin et al., 2013; Moser von Filseck et al., 2015). Several ORPs also have a PI4P-binding PH domain (Hammond and Balla, 2015). Via such domain, ER-anchored ORPs bind adjacent PI4P containing membranes, thus making available PI4P to the ER localized PI 4-phosphatase Sac1. Yeast cells that lack VAP (Scs2;Scs22 double mutants) have greatly elevated levels of plasma membrane PI4P (Stefan et al., 2011).

To gain further insight into the function(s) of VAP in cell physiology, we have studied the effects of the combined absence of VAPA and VAPB in human cells, with an emphasis on the

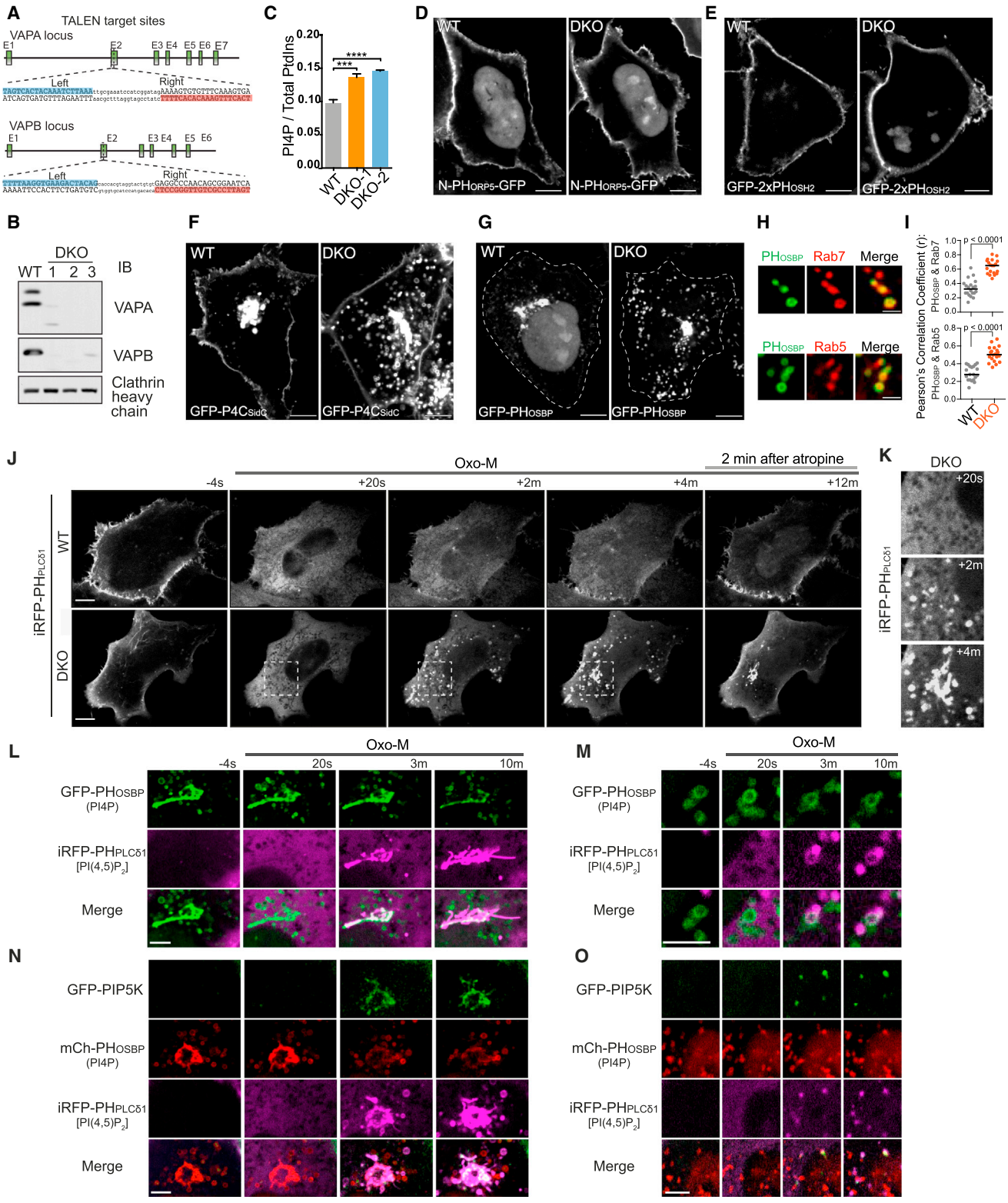

Figure 1. Increased Abundance of PI4P on Endosomes in VAP DKO Cells

(A) Schematic depiction of TALEN targeting sites in exon 2 of human VAPA and VAPB loci. The sequences targeted by the TALEN pairs are highlighted in blue (left arm) and red (right arm) respectively.

(B) Western blot of WT HeLa cells and of three independent VAP DKO HeLa cell lines.

(legend continued on next page)

impact of this perturbation on PI4P dynamics. VAP double knockout (KO) cells have major perturbations in PI4P levels and localization with a surprising very robust accumulation of PI4P on endosomes due to the impaired function of OSBP (and possibly of other ORPs). These changes lead to a disruption of the endosome-Golgi complex boundary that results, at least in part, by dysfunction of the retromer and the WASH complex.

RESULTS

TALEN-Mediated Knockout of Human VAPs

A TALEN-based gene-editing approach (Sanjana et al., 2012) was used to abolish VAP expression in HeLa cells. TALEN pairs specific to exon 2 of VAPA and VAPB, which encodes a stretch of amino acids highly conserved within the MSP domain, were chosen (Figure 1A). This stretch includes the proline whose mutation in VAPB is responsible for ALS8 and abolishes FFAT motif binding (Kim et al., 2010). After validation of gene targeting, three independent VAP double KO cell clones (DKO-1, DKO-2, and DKO-3) were selected where loss of VAPA (a doublet of two splice variants in wild-type cells), and VAPB was confirmed by western blotting (Figure 1B). Importantly, all three clones (referred to henceforth as VAP DKO cells) behaved similarly with regards to the phenotypic defects discussed in this paper.

Increased Abundance of PI4P on Endosomes in VAP DKO Cells

Levels of PI4P relative to total phosphoinositides, as detected by metabolic labeling with [^{3}H]inositol followed by HPLC analysis, were ~40% higher than in wild-type (WT) cells (Figure 1C). No obvious intensity change was observed in the labeling of the plasma membrane by probes that recognize PI4P in this membrane: N-PH$_{ORP5}$-GFP and GFP-2xPH$_{OSH2}$ (Figures 1D and 1E) (Chung et al., 2015; Hammond and Balla, 2015). In contrast, increased fluorescence in VAP DKO cells was observed with probes that recognize intracellular PI4P pools: GFP-P4C$_{SidC}$ and GFP-PH$_{OSBP}$ (Figures 1F and 1G) (Hammond and Balla 2015; Luo et al., 2015). These probes labeled the Golgi complex and, weakly, sparse vesicles throughout the cytoplasm in control cells. In VAP DKO cells, labeling of intracellular vesicles was strikingly stronger, and this difference was abolished by expression of VAPA or VAPB (Figure S1D). PI4P-positive vesicles were also positive for the endosomal markers Rab5 and Rab7 (Figure 1H).

A robust accumulation of PI4P on intracellular vesicles in DKO cells was confirmed by the observation that these vesicles were sites of ectopic PI(4,5)P$_2$ production by type I PIP kinases (Doughman et al., 2003), i.e., the lipid kinases that use PI4P as a substrate. PI(4,5)P$_2$, as revealed by the iRFP-PH$_{PLC\delta1}$ probe, is typically selectively concentrated at the plasma membrane (Hammond and Balla, 2015). This was the case in both untreated control and VAP DKO cells. Upon acute phospholipase C (PLC) activation, as achieved by addition of the muscarinic receptor agonist Oxo-M to cells transiently transfected with the muscarinic acetylcholine receptor (M1R) (Willars et al., 1998), PI(4,5)P$_2$ was massively hydrolyzed, leading to a redistribution of the PI(4,5)P$_2$ probe to the cytosol (Figures 1J and S1F). Such PI(4,5)P$_2$ loss rapidly triggered, as expected, a compensatory burst of PI(4,5)P$_2$ synthesis from PI4P, further accelerated by the addition of the muscarinic receptor antagonist atropine. As assessed by total internal reflection fluorescence (TIRF) microscopy, dissociation and reassociation of iRFP-PH$_{PLC\delta1}$ from and with the plasma membrane had similar kinetics in WT and VAP DKO cells (Figures S1F and S1G). Strikingly, however, while PI(4,5)P$_2$ resynthesis occurred nearly selectively at the plasma membrane in WT cells, it occurred first on internal vesicles and in the Golgi complex in VAP DKO cells (Figures 1J and 1K; Movie S1), consistent with the ectopic abundance of PI4P on such structures. Concomitant analysis of PI4P (GFP-PH$_{OSBP}$) and PI(4,5)P$_2$ (iRFP-PH$_{PLC\delta1}$) during the recovery from Oxo-M stimulation demonstrated direct conversion of PI4P to PI(4,5)P$_2$ on the internal membranes (Figures 1L and 1M) where ectopic presence of a PI4P 5-kinase (PIPKIγ-87kD) was also detected (Di Paolo et al., 2002) (Figures 1N and 1O). Collectively, these observations demonstrated a strong elevation of PI4P on endosomes in VAP DKO cells.

Loss of OSBP and Sac1 Also Results in Increased PI4P Abundance on Endosomes

Recent studies have suggested a model according to which OSBP/ORP family proteins cooperate with the ER-localized PI 4-phosphatase Sac1 to negatively regulate PI4P on subcellular membranes (Chung et al., 2015; Mesmin et al., 2013; Moser von Filseck et al., 2015; Stefan et al., 2011). So far, OSBP has

(C) HPLC analysis of cell extracts showing an increased ratio of PI4P versus total inositol phospholipids in VAP DKO cells relative to WT cells. n = 3 independent experiments. Data are represented as mean ± SEM. WT versus DKO-1, ***p = 0.007; WT versus DKO-2, ****p < 0.0001.

(D–G) Confocal images of WT and VAP DKO cells expressing four different PI4P probes: N-PH$_{ORP5}$-GFP (D) and GFP-2xPH$_{OSH2}$ (E), which label selectively PI4P at the plasma membrane, GFP-P4C$_{SidC}$ (F), which labels PI4P both at the plasma membrane and on internal membranes, and GFP-PH$_{OSBP}$ (G), which labels intracellular PI4P pools. Note the increase of PI4P on vesicular compartments, but no obvious PI4P accumulation at the plasma membrane in VAP DKO cells. Scale bar, 10 μm.

(H and I) Confocal images of VAP DKO cells co-expressing the PI4P probe GFP-PH$_{OSBP}$ and the endosome markers mCh-Rab7 and Rab5-mRFP, revealing the presence of PI4P on endosomes (H). Scale bar, 2 μm. Graph of Pearson's correlation coefficient shows greater colocalization of GFP-PH$_{OSBP}$ with mCh-Rab7 and Rab5-mRFP in VAP DKO cells (I) (n = 20 cells, two-tailed t test).

(J and K) Time-lapse confocal images of WT and VAP DKO cells co-transfected the PI(4,5)P$_2$ probe iRFP-PH$_{PLC\delta1}$ and the muscarinic receptor M1R. Oxo-M (20 μM) was added to cells at time 0 and the M1R antagonist atropine (50 μM) after 10 min. DKO cells show ectopic accumulation of PI(4,5)P$_2$ on intracellular vesicles. The region of the DKO cell indicated by a dashed box in (J) is shown at high magnification in (K). Scale bar, 10 μm. See also Movie S1.

(L–O) High-magnification time-lapse images of VAP DKO cells co-transfected with M1R and the indicated plasmids, showing the appearance of PI(4,5)P$_2$ in the PI4P-rich Golgi complex (L) and on a subset of PI4P-positive vesicles (M) in response to Oxo-M stimulation. PIP5K1γ87 also accumulates in the Golgi complex (N) and on a subset of intracellular vesicles (O) as they become PI(4,5)P$_2$ positive. Scale bar, 5 μm.

See also Figure S1.

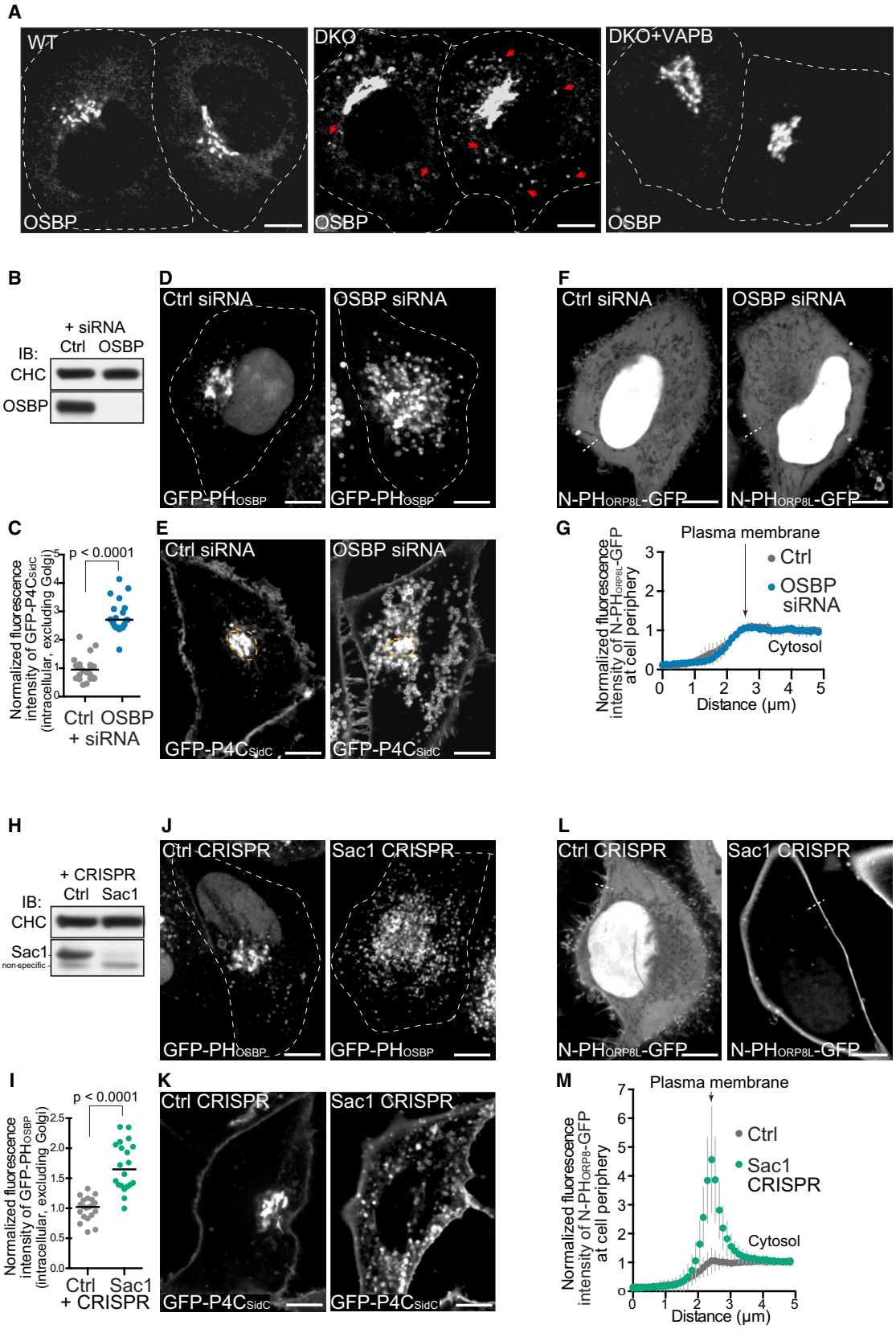

(legend on next page)

been reported to associate primarily with Golgi membranes (Mesmin et al., 2013). However, not only the PH domain-only of OSBP (a PI4P probe) (Figure 1G), but endogenous OSBP itself displayed a robust accumulation on endosomes in VAP DKO cells and such accumulation was rescued by expression of VAP (Figure 2A). OSBP is a FFAT motif containing VAP interactor. Thus, in the absence of VAP, the accumulation of PI4P on endosomes may at least in part reflect the impaired ability of OSBP delivering PI4P to Sac1 for degradation. Supporting this hypothesis, RNAi-mediated knockdown (KD) of OSBP resulted in a major increase of PI4P on endosomes as revealed by the PI4P probes GFP-PH_{OSBP} and GFP-$P4C_{SidC}$ (Figures 2B–2E). Note that OSBP KD did not produce an obvious change in PI4P abundance at the plasma membrane, as assessed by GFP-$P4C_{SidC}$ and also by N-PH_{ORP8L}, a low-affinity PI4P probe that labels selectively the plasma membrane pool of PI4P (Figures 2F and 2G) (Chung et al., 2015). This was not unexpected, as key players in the regulation of plasma membrane PI4P are ORP5 and ORP8, two ORPs that are anchored at the ER independently of VAP (Chung et al., 2015).

Importantly, knockout (KO) of Sac1 by CRISPR/Cas9 (Figures 2H and S2A; Supplemental Experimental Procedures) resulted in a very robust increase in GFP-$P4C_{SidC}$ signal both at the plasma membrane and on intracellular membranes (Figure 2K), indicating a functional partnership of Sac1 with both OSBP and ORP5/ORP8. This was confirmed by the expression in control and Sac1 KO cells of GFP-PH_{OSBP} (Figure 2J) and N-PH_{ORP8L}-GFP (Figures 2L and 2M), which recognize PI4P selectively on internal membranes and in the plasma membrane (Chung et al., 2015), respectively. The collective signal generated by these probes was elevated in Sac1 KO cells (Figure S2B).

We conclude that VAP plays a critical role in the downregulation of PI4P on endosomes at least in part by making accessible PI4P to ER localized phosphatase Sac1.

Loss of VAP Disrupts Traffic between Endosomes and the Golgi Complex

While the occurrence of pleotropic defect can be expected in VAP DKO cells, given the multiple interactors of VAP (Murphy and Levine, 2016), the abnormal abundance of PI4P on endosomes prompted us to focus on defects in these compartments. A profound disruption of traffic at the endosome-Golgi interface was observed. As revealed by immunofluorescence, TGN46, a TGN protein in WT cells, was partially scattered throughout the cytoplasm of DKO cells as small puncta that colocalized with endosomal markers, such as EEA1 and the retromer subunit Vps35 (Bonifacino and Rojas, 2006; Hierro et al., 2007; Seaman et al., 1998) (Figures 3A–3C). Likewise, in DKO cells, marker proteins of the *trans*-Golgi, ST-mRFP, and GalT-EGFP (mRFP and EGFP fusions of sialyltransferase and galactosyltransferase fragments, respectively) (Cole et al., 1996; Schaub et al., 2006), were observed on puncta that colocalized with Rab5, Rab7, and the retromer component VPS29 (Figures 3D–3F). A similar scattered distribution was observed previously for endogenous galactosyltransferase in VAPA and VAPB double knock down cells (Peretti et al., 2008). No change was observed in the localization of several other Golgi complex proteins tested, such as GOLPH3 (Figure 3G), GRASP55 (Figure 3A), Golgin97, GM130, GRASP65, and P230 (Figures S3A and S3B), indicating that absence of VAP does not affect the Golgi complex globally.

Endosomes and the Golgi complex are continuously interconnected by bidirectional traffic. The accumulation of proteins of distal Golgi compartments in endosomes of VAP DKO cells suggested that VAP is required for proper transport between these two compartments. One such mechanism involves the retromer, a coat that controls exit from endosomes of Golgi-bound proteins by generating tubular buds and selecting their cargo, such as the cation-independent mannose-6-phosphate receptor (CI-MPR) (Bonifacino and Rojas, 2006; Burd and Cullen, 2014; Seaman et al., 1998). This receptor shuttles between the Golgi complex and endosomes and is also present at low levels at the plasma membrane. In WT cells, CI-MPR is primarily enriched in the Golgi complex in a retromer-dependent way (Bonifacino and Rojas, 2006). Accordingly, following 1 hr incubation of WT cells in the presence of an antibody that recognizes the extra cytosolic portion of CI-MPR exposed at the cell surface, the internalized antibody had primarily accumulated in the Golgi complex. In contrast, the antibody had accumulated only in peripheral endosomal vesicles in DKO cells, consistent with retromer dysfunction (Figure 3H), and this defect was rescued by re-expression of either VAP (Figures S3C and S3D).

Figure 2. Loss of OSBP and Sac1 Results in Increased PI4P Abundance on Endosomes

(A) Immunofluorescence revealing enhanced localization of endogenous OSBP on intracellular vesicles in VAP DKO cells (red arrowheads) and rescue of this change by exogenously expressed WT VAPB. Scale bar, 10 μm.

(B) Western blot of WT HeLa cells transfected with the indicated siRNAs showing depletion of OSBP protein in OSBP siRNA transfected cells.

(C–G) Confocal images of WT cells transfected with control or OSBP siRNA and expressing three distinct PI4P probes: GFP-PH_{OSBP} (D), which label selectively internal PI4P pools, GFP-$P4C_{SidC}$ (E), which label both internal and plasma membrane PI4P pools, and N-PH_{ORP8L}-GFP (F), a low-affinity "sensor" of plasma membrane PI4P that remains primarily in the cytosol/nucleus under control conditions. In OSBP siRNA-treated cells, GFP-$P4C_{SidC}$ (E) and GFP-PH_{OSBP} (D) accumulate in vesicular compartments. No increase of PI4P in the plasma membrane is detected by any of these probes. Scale bar, 10 μm. (C and G) Quantifications of the vesicular fluorescence of GFP-PH_{OSBP} and of the plasma membrane/cytosol N-PH_{ORP8L}-GFP fluorescence ratio based on line scans as exemplified in (F) (n = 20 cells for cells treated with control or OSBP siRNAs, two-tailed t test).

(H) Western blot of WT cells transfected with CRISPR/Cas9s constructs as indicated, showing the depletion of Sac1 protein in Sac1 CRISPR/Cas9 transfected cells.

(I–M) Confocal images of WT HeLa cells transfected with control or Sac1 CRISPR/Cas9 and expressing the same three distinct PI4P probes used for fields (D–F). In Sac1 CRISPR/Cas9-treated cells, GFP-PH_{OSBP} (J) and GFP-$P4C_{SidC}$ (K) show a robust labeling of vesicles, and N-PH_{ORP8L}-GFP redistributes from the cytosol/nucleus to the plasma membrane (L), signaling a major increase of PI4P in all these membranes. Scale bar, 10 μm. (I and M) Quantifications of the vesicular fluorescence of GFP-PH_{OSBP} and of the plasma membrane/cytosol N-PH_{ORP8L}-GFP fluorescence ratio based on line scans (n = 20 cells for each genotype in I, two-tailed t test).

See also Figure S2.

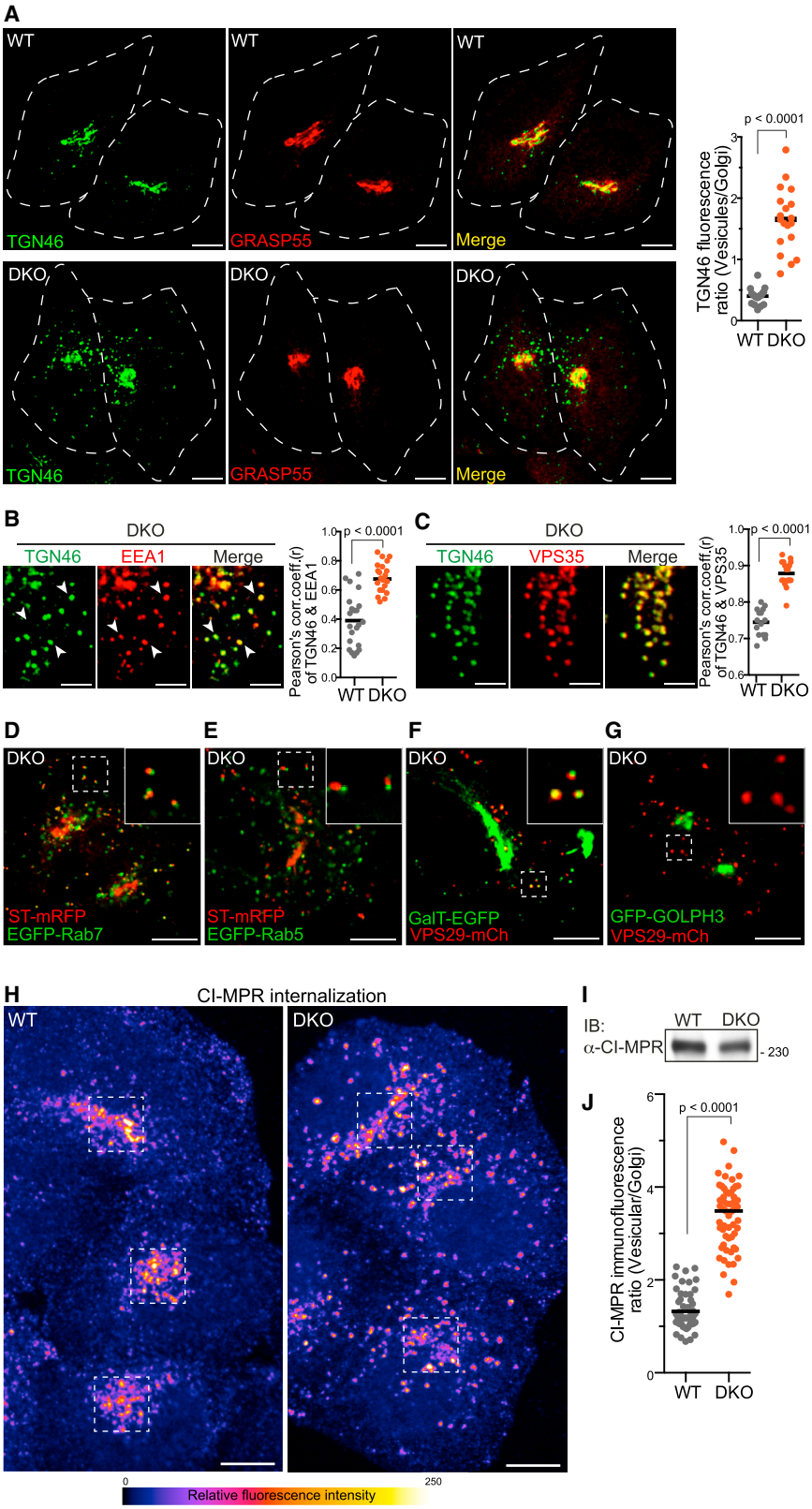

Figure 3. Defects in Endosomes-to-Golgi Traffic in VAP DKO Cells

(A) TGN46 and GRASP55 immunofluorescence showing the Golgi localization of TGN46 in WT cells and its scattered distribution in the cytoplasm of VAP DKO cells. Scale bar, 10 μm. The graph at right shows the ratio of the punctate TGN46 fluorescence throughout the cytoplasm excluding the Golgi region, versus the TGN46 fluorescence within the Golgi region (n = 19 cells for each genotype, two-tailed t test).

(B and C) Close apposition of TGN46 and endosomal markers (EEA1 and VPS35) in DKO cells. Scale bar, 5 μm. Graphs of the Pearson's correlation coefficient shows greater colocalization of TGN46 with EEA1 and VPS35 in VAP DKO cells than in WT (n = 22 cells for each genotype in B, n = 15 cells for WT and 17 cells for VAP DKO in C, two-tailed t test).

(D–E) Snapshots from live confocal imaging of VAP DKO cells showing juxtaposition of the *trans*-Golgi marker ST-mRFP with Rab7-EGFP (D) and Rab5-EGFP (E) positive endosomes (the mRFP and EGFP signals, which are acquired sequentially, are slightly shifted due to the high motility of the organelles). The retromer subunit VPS29-mCh colocalizes with scattered vesicles that are positive for the *trans*-Golgi marker GalT-EGFP (F), but shows no overlap with the *cis*/medial-Golgi GFP-GOLPH3 that remains concentrated in the Golgi (G). Scale bar, 10 μm.

(H–J) (H) Immunofluorescence of internalized (1 hr) anti-CI-MPR antibody (pseudo colored). The internalized antibody is enriched in the perinuclear region corresponding to the TGN in WT cells, but remains disperse in peripheral puncta in VAP DKO cells (note those outside the squares). Scale bar, 10 μm. (I) Western blots of WT and VAP DKO cells revealing no major change of CI-MPR expression levels. (J) Ratio between the punctate fluorescence outside and inside squares (10 × 10 μm^2) centered on the Golgi complex area (see dashed squares) (n = 55 for WT and 57 for DKO cells, two-tailed t test).

See also Figure S3.

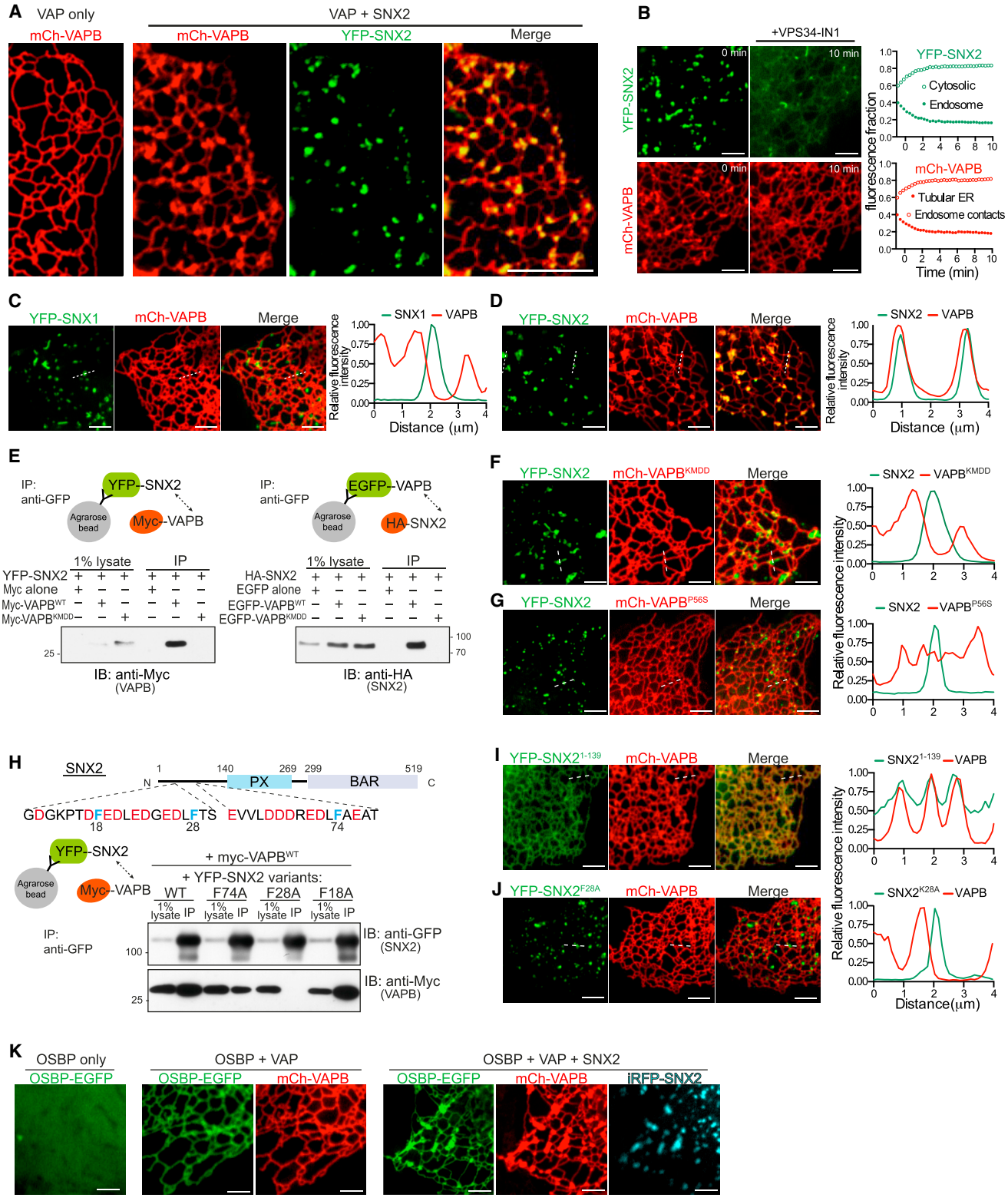

Figure 4. Endosome-ER Tethering via an SNX2-VAPB Interaction

(A) Confocal images of COS-7 cells expressing mCh-VAPB alone, or co-expressing YFP-SNX2 and mCh-VAPB, showing the enrichment of mCh-VAP at YFP-SNX2-positive endosomes. Scale bar, 10 μm.

(legend continued on next page)

A Physical Link between the Retromer and VAP

The ER makes contacts with endosomes, including VAP-dependent contacts (Alpy et al., 2013; Raiborg et al., 2015; Rocha et al., 2009). As some of the ER-endosome contacts occur at retromer-dependent budding sites (Rowland et al., 2014), we hypothesized that the retromer itself may interact with VAP. Inspection of a high-throughput VAP interactome (Huttlin et al., 2015) revealed as one of the top hits SNX2, a component of the membrane deformation subcomplex of the retromer (Bonifacino and Rojas, 2006). The potential significance of this finding was assessed by transfection experiments (and thus overexpression) in COS-7 cells, which are optimally suited for the imaging of ER architecture.

When expressed independently, YFP-SNX2 had the punctate localization that reflects its PI3P-dependent (via its PX domain) localization on endosomes (Burd and Cullen, 2014), while mCh-VAPA and mCh-VAPB had a diffuse distribution throughout the ER as expected. When YFP-SNX2 was co-expressed with either mCh-VAPA or mCh-VAPB, focal accumulation of VAP was observed at SNX2-positive endosomes (Figures 4A, 4D, and S4A). Such accumulation did not occur upon expression of other retromer proteins, such as SNX5, SNX6, or even of SNX1, the paralogue of SNX2 (Figures S4C, S4D, and 4C, respectively). Furthermore, acute depletion of endosomal PI3P by pharmacological inhibition of the type III PI 3-kinase VPS34 with VPS34-IN1 (Bago et al., 2014), not only resulted in the dissociation of SNX2 from endosomes to the cytosol (Burd and Cullen, 2014), as expected, but also in the dispersion of VAP, which re-acquired its uniform distribution throughout the ER (Figure 4B; Movie S2).

Further experiments demonstrated a direct interaction between SNX2 and VAP. First, SNX2 and VAPB were coprecipitated from detergent solubilized cell extracts (Figure 4E). In contrast, neither coprecipitation, as assessed by western blotting (Figure 4E) or mass spectrometry (Figures S4E and S4F) of the immunoprecipitates, nor coclustering, as assessed by microscopy (Figure 4F), was observed when WT VAPB was replaced by an FFAT motif-binding-deficient VAPB mutant (double K87D and M89D mutations, referred to as $VAPB^{KMDD}$) (Kaiser et al., 2005). The ALS-associated P56S mutation of VAPB, known to result in the misfolding of its FFAT-binding domain (the MSP domain), also inhibited coclustering (Figure 4G). Second, coclustering of SNX2 and VAPB required the N-terminal region of SNX2 (Figures 4I and S4B), which contains amino acid stretches reported to fit an FFAT-like consensus (Murphy and Levine, 2016) (Figure 4H). Mutation of phenylalanines in these motifs abolished (F28) or strongly reduced (F74) the interaction, as assessed by coprecipitation and coclustering (Figures 4H and 4J).

These findings reveal a direct functional link between VAP and retromer. As VAP occurs as a dimer that can further oligomerize (Kaiser et al., 2005; Kim et al., 2010), the binding of VAP to SNX2 may help bring OSBP in proximity of the retromer. Accordingly, we observed that cotransfected OSBP-EGFP, iRFP-SNX2, and mCherry-VAPB colocalized at the same hotspots (Figure 4K).

Accumulation of Actin on Endosomes Leading to Actin Comets

Live-cell imaging showed that endosome-Golgi hybrid vesicles of DKO cells had very high mobility. As retromer budding is assisted by a transient local burst of actin (Puthenveedu et al., 2010), we examined actin organization in DKO cells. F-actin staining with fluorescent phalloidin revealed loss of stress fibers (the predominant form of actin in control HeLa cells, Figure 5A) and presence of numerous and prominent actin foci or elongated structures located deep in the cytoplasm (Figures 5B and S5B). These changes could be rescued by exogenously expressing WT VAPA or VAPB, but not $VAPB^{KMDD}$ or by expression of the MSP domain of VAPB alone, which is not anchored to the ER (Figures S5D–S5G). No major changes were observed in the microtubule cytoskeleton (Figure S5A).

The actin phenotype revealed by phalloidin was confirmed by observations of live cells expressing the GFP- or mCherry-tagged calponin homology domain of utrophin ($CH_{Utrophin}$), an F-actin reporter that also allowed identification of these structures as actin comets (Ferguson et al., 2009). Actin comets, also called actin tails, are bundles of highly dynamic actin that push organelles within the cytoplasm as a result of actin polymerization at the organelle interface and actin depolymerization at the opposite end. Consistent with a high turnover rate of actin in these structures, they disappeared more rapidly than stress

(B) Confocal images of a COS-7 cell co-expressing YFP-SNX2 and mCh-VAPB upon treatment with the VPS34 inhibitor VPS34-IN1 (1 μM). The dissociation of YFP-SNX2 from endosomes correlates with the dispersal of mCh-VAPB throughout the ER. Quantification is shown at right. Scale bar, 5 μm. See also Movie S2.
(C and D) Confocal images and line scan analysis of COS-7 cells overexpressing YFP-SNX1 and mCh-VAPB (C), or YFP-SNX2 and mCh-VAPB (D), showing that mCh-VAPB coclusters selectively with YFP-SNX2 but not with YFP-SNX1. Scale bar, 5 μm.
(E) Extracts of HeLa cells transfected with the constructs indicated were subjected to anti-GFP immunoprecipitation (IP) and then processed for SDS-PAGE and immunoblotting (IB) with anti-Myc or anti-HA antibodies.
(F and G) Confocal images and line scan analysis of COS-7 cells co-expressing YFP-SNX2 and either the FFAT motif-binding-deficient mutant $mCh\text{-}VAPB^{KMDD}$ (double mutant *K87D M89D*) (F), or the ALS8 mutant $mCh\text{-}VAPB^{P56S}$ (G), showing that mCherry fluorescence remains diffuse throughout the ER tubular network and does not cocluster with YFP-SNX2. Scale bar, 5 μm.
(H) Top: SNX2 domain structure. Note the presence of sequences containing phenylalanine residues and acidic amino acids. Bottom: extract of HeLa cells transfected with $myc\text{-}VAPB^{WT}$ and WT or mutant YFP-SNX2 were subjected to anti-GFP immunoprecipitation (IP) and then processed for SDS-PAGE and immunoblotting (IB) with anti-GFP and anti-Myc antibodies.
(I and J) Confocal images and line scan analysis of COS-7 cells co-expressing mCh-VAPB and either YFP-tagged N-terminal fragment of SNX2 ($YFP\text{-}SNX2^{1–139}$) (I), or $YFP\text{-}SNX2^{F28A}$ (J). $YFP\text{-}SNX2^{1–139}$, which lacks the endosome binding sites but contains the FFAT-like motif, colocalizes with VAPB throughout the ER. $YFP\text{-}SNX2^{F28A}$ localizes to endosomes but fails to cocluster with VAPB. Scale bar, 5 μm.
(K) Confocal images of COS-7 cells showing that OSBP-EGFP has a predominant diffuse localization when overexpressed alone, is recruited to the ER membrane when co-overexpressed with mCh-VAPB, and is also co-enriched with mCh-VAPB at iRFP-SNX2-positive hotspots when coexpressed with both these proteins. Scale bar, 5 μm.
See also Figure S4.

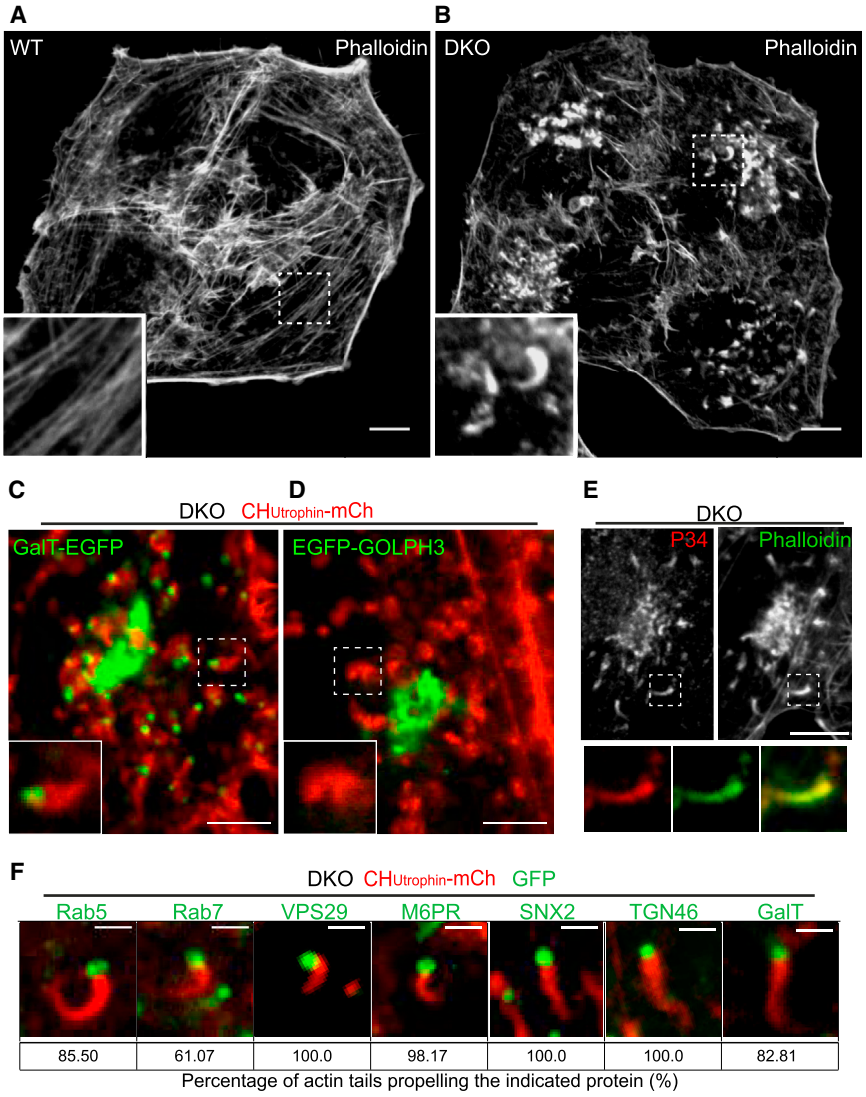

Figure 5. Drastic Perturbation of Actin Organization in VAP DKO Cells

(A and B) Phalloidin staining of WT and VAP DKO cells showing loss of stress fiber and accumulation of actin comets in DKO cells. Insets: high magnification of the regions enclosed by dashed boxes. Scale bar, 10 μm.

(C and D) Confocal images of DKO cells showing presence of a *trans*-Golgi marker GalT-EGFP (C), but not of a *cis*/medial-Golgi protein EGFP-GOLPH3 (D), at the tips of actin comets visualized by $CH_{Utrophin}$-mCh. Insets show actin comets at high magnification. Scale bar, 10 μm.

(E) Colocalization of Arp2/3 (p34-Arc subunit) immunofluorescence and phalloidin staining in VAP DKO cells. Scale bar, 10 μm.

(F) Confocal images of DKO cells showing presence of endosomal Rabs (Rab5-EGFP; Rab7-EGFP), retromer subunits (YFP-VPS29 and YFP-SNX2), the retromer cargo GFP-CD-M6PR and *trans*-Golgi markers (TGN46-GFP, GalT-EGFP) at the tips of actin tails visualized by $CH_{Utrophin}$-mCh. Scale bar, 2 μm. Numbers below the micrographs indicate the percentage of actin tails propelling the indicated protein (n = 200 from ten cells for Rab5, n = 131 from eight cells for Rab7, n = 99 from six cells for VPS29, n = 109 from ten cells for CD-M6PR, n = 82 from five cells for TGN46, n = 64 from four cells for GalT).

See also Figure S5 and Movie S3.

fibers upon treatment with latrunculin, which impairs actin polymerization (Figure S5C) (Puthenveedu et al., 2010). Comets tips were positive for endosomal Rabs (Rab5, Rab7), the *trans*-Golgi marker proteins TGN46-EGFP and GalT-EGFP, the retromer cargo M6PR, and retromer components (such as Vps29 and SNX2) (Figures 5C and 5F; Movie S3), thus indicating that the high motility of the endosome-Golgi hybrid vesicles is due to their property to nucleate actin.

Actin Comets of VAP DKO Cells Are Nucleated by WASH

Previously described actin comets propelling endogenous organelles are nucleated by N-WASP, a Wiskott-Aldrich syndrome family member. Such comets are typically observed under conditions where $PI(4,5)P_2$ ectopically accumulates on intracellular vesicles (Rozelle et al., 2000). Like N-WASP and $PI(4,5)P_2$-dependent actin tails, actin tails of VAP DKO cells were Arp2/3 positive (Figure 5E). However, they were generally more centrally localized in the cell (Figure 5B). Furthermore, their tips were negative for N-WASP and for endocytic proteins typically found at the tips of $PI(4,5)P_2$-dependent tails including clathrin coat-associated factors such as SNX9 (Nandez et al., 2014) (Figures S6A and S6B). This difference was directly demonstrated in VAP DKO cells upon overexpression of the PI4P 5-kinase PIP5K1γ87 (Di Paolo et al., 2002) to generate $PI(4,5)P_2$-dependent comets. In these cells, PIP5K1γ87 was only observed at the tip of a subset of actin tails, which were thick and long, clearly distinct from the shorter, thinner actin comets induced by loss of VAP (Figures S6C and S6D). This prompted us to explore the potential presence of WASH, another member of the Wiskott-Aldrich protein family, at the tips of tails in VAP DKO cells (Derivery et al., 2009; Gomez and Billadeau, 2009). WASH is part of a complex that interacts with the retromer via its FAM21 subunit and that assists the retromer-dependent budding reaction by nucleating actin at bud sites on endosomes (Harbour et al., 2012).

Immunofluorescence revealed the presence of both WASH and FAM21 at all comet tips in VAP DKO cells (Figures 6A and 6B). This was confirmed by live microscopy of DKO cells co-expressing YFP-FAM21 with CH_{UTR}-mCh (Figure 6C; Movie S4). Accordingly, KD of either WASH or FAM21 (FAM21 KD resulted in the concomitant loss of WASH) suppressed the actin tail phenotype in VAP DKO cells (Figures 6F–6I). Consistent with the hybrid endosome-Golgi nature of organelles at the tip of the tails, the

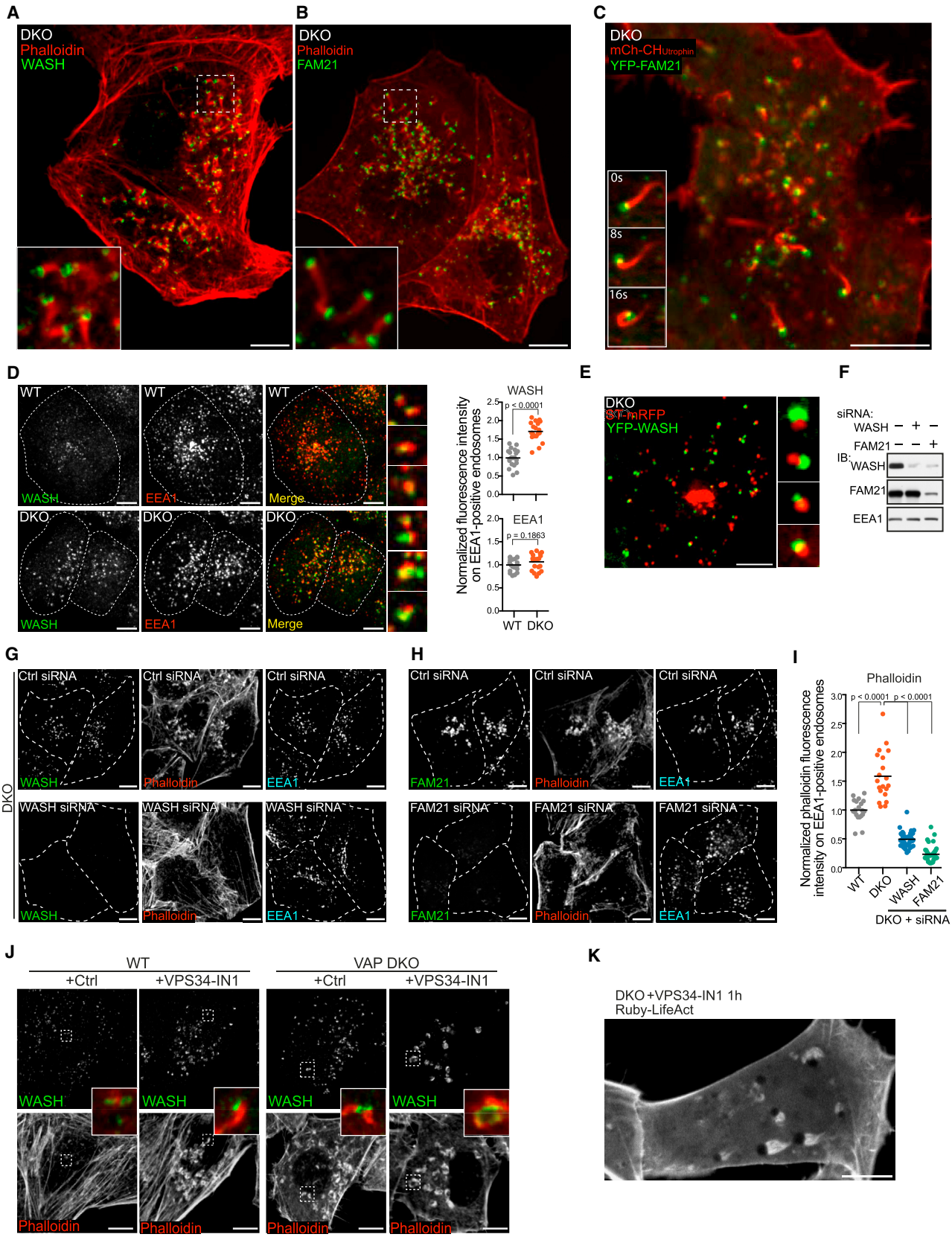

(legend on next page)

endosomal marker EEA1 (Figure 6C) and the Golgi marker ST-mRFP (Figure 6E) were juxtaposed to WASH. Additionally, morphometric analysis of immunofluorescence images showed that pixel intensity for WASH immunoreactivity, but not for EEA1 immunoreactivity, increased in VAP DKO cells relative to WT cells (Figures 6C and 6D), revealing a greater pool of assembled WASH.

PI4P and WASH-Mediated Actin Nucleation

Actin nucleation by WASH at retromer-dependent budding sites on endosomes is tightly controlled in WT cells (Puthenveedu et al., 2010). Exaggerated actin nucleation in VAP DKO cells could result from an altered balance between "on" and "off" signals underlying such nucleation.

In the case of N-WASP-dependent actin comets, it is the balance between PI(4,5)P_2 synthesis and dephosphorylation that controls actin nucleation (Nandez et al., 2014; Rozelle et al., 2000). Thus, we considered a role of endosomal phosphoinositides in the enhanced nucleation of WASH-dependent actin resulting from the lack of VAP. We ruled out PI3P, as inhibition of its synthesis on endosomes via the VPS34 inhibitor VPS34-IN1 (Bago et al., 2014) did not inhibit actin nucleation and in fact it stimulated it: it enhanced WASH recruitment both in WT and in VAP DKO cells, with the formation of actin comets in WT cells and exaggeration of actin on endosomes of DKO cells (Figure 6J). In some cells, where the inhibitor resulted in dramatically enlarged endosomes, actin tails were particularly prominent (Figure 6K; Movie S5).

To assess a potential role of abnormally elevated PI4P, we examined whether enhanced WASH-dependent actin nucleation could be mimicked by the loss of OSBP, which, as shown above, also results in such elevation. In OSBP KD cells, where endosomes (EEA1) became more clustered (Figure S7G), a robust enhancement of WASH immunoreactivity was detected on these organelles, along with the presence of assembled actin (Figures 7A and 7B), which at close inspection was represented by actin tails (Figures 7C and 7D; Movie S6). The presence not only of WASH, but also of FAM21, the *trans*-Golgi marker protein GalT-EGFP, Rab5, and Rab7 at the tips of the tails confirmed their similarity to the tails observed in VAP DKO cells (Figures 7C and 7D). Importantly, the additional KD of WASH in OSBP KD cells abolished the internal actin foci (Figure 7E). Further supporting a role of a complex involving OSBP, VAP and the retromer in the negative regulation of PI4P on endosomes, the KD of SNX2 also resulted in an increase of intracellular actin very similar to that produced by the KD of OSBP (Figures 7F–7J).

WASH-Mediated Actin Nucleation Is Impaired by the Knockdown of Type II PI 4-Kinases

If endosomal PI4P is required for the formation of actin tails in VAP DKO cells, impairment of PI4P synthesis should impair their formation. Mammalian genome encodes four PI 4-kinases. Neither inhibition of PI4KIIIα, which acts primarily at the plasma membrane (Nakatsu et al., 2012) (with the A1 compound) (Bojjireddy et al., 2014), nor inhibition of PI4KIIIβ, which acts primarily in the Golgi complex (Godi et al., 1999) (with the PIK-93 compound) (Knight et al., 2006), had a major impact on actin comets and on the presence of PI4P on the endosome-*trans*-Golgi vesicles, although they reduced PI4P levels at the plasma membrane and the Golgi complex respectively, as expected (Figures S7A–S7D). No specific inhibitors are available for the two type II PI 4-kinases PI4KIIα and PI4KIIβ, which have a predominant endosomal localization (Balla et al., 2002) and thus could be the key players in PI4P generation on the hybrid endosome-*trans*-Golgi organelles. Importantly, GFP fusions of these two kinases and PI4P probe were detected at the tips of actin comets in DKO cells, supporting this possibility (Figure 7K; Movie S7). Strong reduction of the endogenous levels of these two kinases by small interfering RNA (siRNA)-dependent KD, as validated by western blotting (Figure 7O), drastically decreased the PI4P probe signal (GFP-P4C_{SidC} and GFP-PH_{OSBP}) on hybrid endosome-Golgi vesicles (Figures 7N and 7P). Correspondingly, the KD of the two PI4KIIs decreased the abundance of phalloidin-detectable actin foci in VAP DKO cells and restored abundance of stress fibers (Figures 7L and 7M, top fields). It also reversed the intense enrichment of WASH immunoreactivity on EEA1-positive endosomes (Figures 7L and 7M, bottom fields). These results strongly support a role of PI4P in WASH-dependent actin nucleation and show that PI4KIIα and PI4KIIβ are the enzymes responsible for the generation of this PI4P pool.

DISCUSSION

We have shown that VAP-dependent ER-endosome contacts involving the retromer subunit SNX2 and OSBP have an impact

Figure 6. Actin Comets in VAP DKO Cells Are Nucleated by WASH

(A and B) WASH (A) and FAM21 (B) immunofluorescence at tips of actin tails visualized by phalloidin staining in VAP DKO cells. Scale bar, 10 μm.

(C) Live confocal images of a VAP DKO cell expressing YFP-FAM21 and the actin marker CH_{UTR}-mCh. Insets show at high magnification a time series of an actin comet tail propelling a FAM21-positive vesicle. Scale bar, 10 μm. See also Movie S4.

(D) Enhanced abundance of WASH on EEA1-posotivie endosomes in DKO cells (as quantified at right, n = 20 cells for each genotype, two-tailed t test). Scale bar, 10 μm. Merged images of high magnification views of individual endosomes are shown at right.

(E) Confocal image (high-magnification gallery at right) of a VAP DKO cell showing apposition of EGFP-WASH and of the *trans*-Golgi marker ST-mRFP. Scale bar, 10 μm.

(F) Western blot proving KD of WASH and FAM21. Note that FAM21 KD results in a concomitant loss of WASH.

(G–I) Phalloidin staining and immunofluorescence of DKO cells transfected with the indicated siRNAs, showing that loss of WASH (G) and FAM21 fluorescence (H) correlates with the loss of actin foci (comets) on endosomes. Scale bar, 10 μm. The normalized phalloidin fluorescence on EEA1-positive areas is quantified in (I).

(J) WASH immunofluorescence and phalloidin staining of WT and DKO cells treated with the VPS34 inhibitor VPS34-IN1 (1 μM) or solvent control (DMSO). VPS34-IN1 induces an increase of WASH and actin at the endosomal surface of both WT and DKO cells. Scale bar, 10 μm.

(K) Confocal image of VAP DKO cells expressing actin probe Ruby-LifeAct treated with VPS34 inhibitor VPS34-IN1 (1 μM) for 1 hr, showing dramatically exaggerated actin tails propelling strikingly enlarged endosomes. Scale bar, 10 μm.

See also Figure S6 and Movie S5.

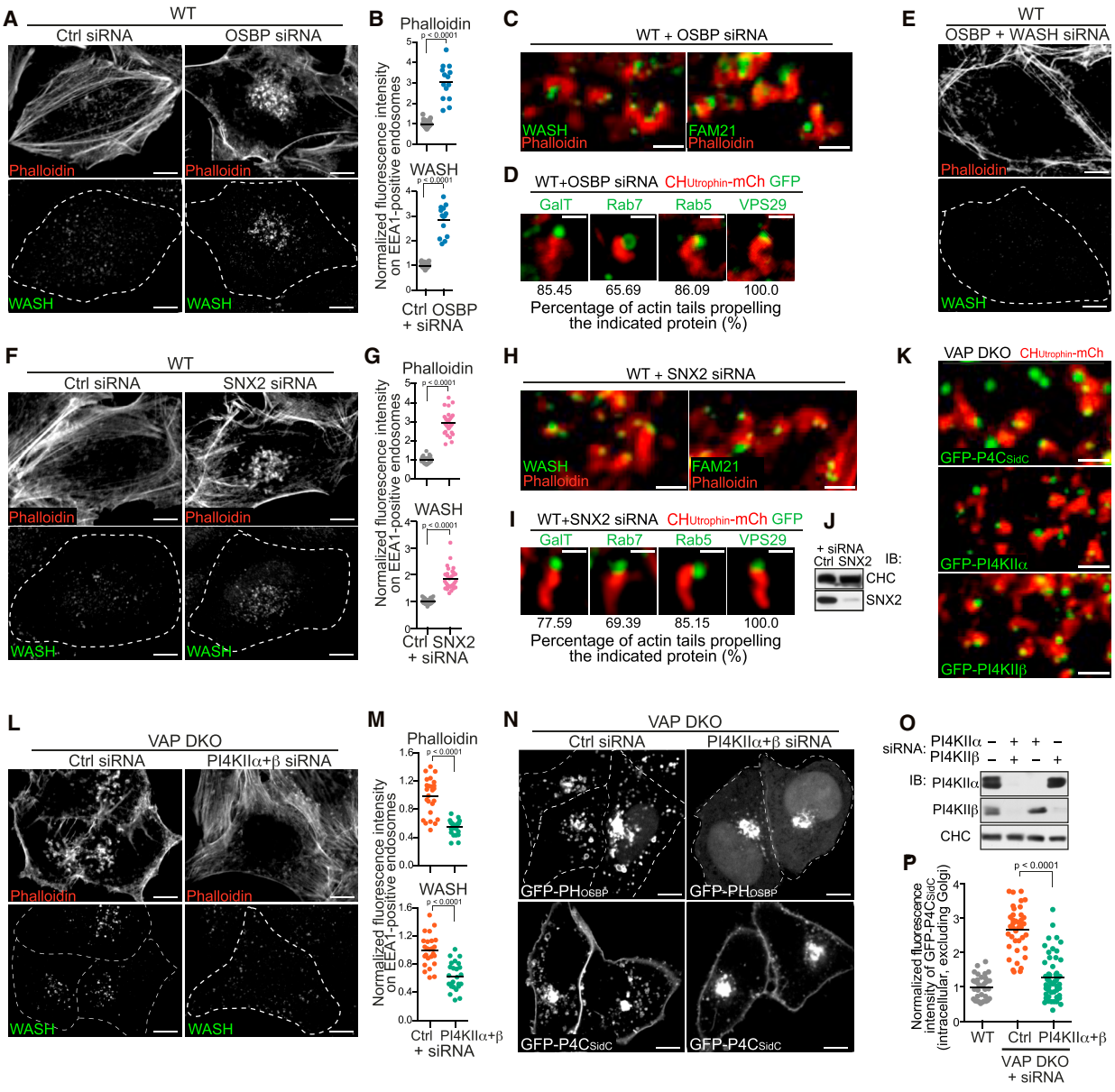

(legend on next page)

on PI4P dynamics on endosomes. Via this action, VAP affects the interrelated functions of the retromer and WASH on these organelles, providing a new example of cross-talk between organelles mediated by direct contacts not leading to fusion.

The robust increase of PI4P in response to the lack of VAP is consistent with growing evidence that VAP helps, primarily via OSBP/ORP proteins, to generate bridges between the ER and other membranes that make accessible PI4P to the ER localized PI4P phosphatase Sac1. This may occur via delivery of PI4P to the ER by the transport activity of these proteins (Chung et al., 2015; Mesmin et al., 2013; Moser von Filseck et al., 2015) or, as proposed by others, by in *trans* action of Sac1 on the adjacent membrane (Dickson et al., 2016; Stefan et al., 2011). In yeast, deletion of the two VAP homologs (Scs2 and Scs22) results in strong PI4P elevations, with the bulk of excessive PI4P being localized at the plasma membrane (Stefan et al., 2011). Loss of VAP results in increased PI4P levels also in mammalian cells. However, PI4P increase does not occur at the plasma membrane, possibly because two ORP proteins that do not require VAP for ER anchoring, ORP5 and ORP8, function in the negative regulation of PI4P at the ER-plasma membrane interface (Chung et al., 2015). Our results show in VAP DKO cells the major increase of PI4P occurs on intracellular membranes (endosomes) and implicates impaired recruitment of OSBP in this change. OSBP was shown to control PI4P at the Golgi complex (Mesmin et al., 2013), but our study suggests its additional role at endosomes. PI4P elevation on endosomes in VAP DKO cells cannot be explained by a spillover of PI4P from the Golgi complex, as it is not rescued by the pharmacological inhibition of PI4KIIIβ, the major player in the synthesis of PI4P in the Golgi complex. It is abolished, however, by the KD of PI4KIIα and PI4KIIβ, the two PI4Ks with an endosomal site of action (Burgess et al., 2012; Henmi et al., 2016; Minogue et al., 2006; Ryder et al., 2013). Other ORPs likely cooperate with OSBP in the actions reported here (Olkkonen and Levine, 2004), but the effects produced by the KD of OSBP strongly indicate its major involvement.

The increase of PI4P on endosomes observed in VAP DKO cells was accompanied by an accumulation of proteins of the *trans*-Golgi on endosomes, suggesting that the efficiency of sorting mechanisms that control traffic between the two organelles is compromised. This was consistent with the link that we have found between VAP and the retromer subunit SNX2. The function of retromer in fission of membrane tubules from endosomes is tightly coupled to actin nucleated by WASH (Derivery et al., 2009; Gomez and Billadeau, 2009; Puthenveedu et al., 2010). It was therefore of interest that a most striking phenotype of DKO cells was a robust reorganization of actin, with the loss of stress fibers and the abundant presence of actin comets, which were nucleated by WASH on the

Figure 7. A Protein Network Involving Type II PI 4-Kinases and the VAP Interactors OSBP and SNX2 Is Implicated in WASH-Dependent Actin Comets Formation

(A and B) Increased abundance of assembled actin (phalloidin) and WASH immunofluorescence on intracellular organelles in OSBP KD cells (A). Scale bar, 10 μm. Normalized fluorescence intensity of WASH and phalloidin on the region occupied by EEA1-positive endosomes (see Figure S7G) is quantified in (B) (n = 20 cells for either control or OSBP siRNAs, two-tailed t test).

(C) WASH and FAM21 immunofluorescence at the tips of actin tails visualized by phalloidin staining in OSBP siRNA-treated cells. Scale bar, 2 μm. See also Movie S6.

(D) Live confocal images of OSBP siRNA-treated cells showing presence of endosomal Rabs (Rab5-EGFP; Rab7-EGFP), retromer subunits (YFP-VPS29), and a *trans*-Golgi marker (GalT-EGFP) at the tips of actin tails visualized by CH_{UTR}-mCh. Scale bar, 2 μm. Numbers below each image indicate the percentage of actin tails propelling the indicated proteins (n = 115 from seven cells for Rab5, n = 93 from five cells for Rab7, n = 99 from five cells for VPS29, n = 110 from eight cells for GalT).

(E) Immunofluorescence of WASH and phalloidin staining in WT cells transfected with OSBP and WASH siRNA, showing that loss of WASH fluorescence correlates with the loss of actin foci. Scale bar, 10 μm.

(F and G) (F) Increased abundance of assembled actin (phalloidin) and WASH immunofluorescence on intracellular organelles in SNX2 knockdown cells. Scale bar, 10 μm. Normalized fluorescence intensity of WASH and phalloidin on the region occupied by EEA1-positive endosomes (see Figure S7H) is quantified in (G) (n = 20 cells for either control or SNX2 siRNAs, two-tailed t test).

(H) WASH (left) and FAM21 (right) immunofluorescence at the tips of actin tails visualized by phalloidin staining in SNX2 siRNA-treated cells. Scale bar, 2 μm.

(I) Live confocal images of SNX2 siRNA-treated cells showing presence of endosomal Rabs (Rab5-EGFP; Rab7-EGFP), retromer subunits (YFP-VPS29), and *trans*-Golgi markers (GalT-EGFP) at the tips of actin comets visualized by CH_{UTR}-mCh. Scale bar, 2 μm. The percentage of actin tails whose tips are positive for the indicated proteins is shown under each image (n = 101 from six cells for Rab5, n = 114 from six cells for Rab7, n = 97 from five cells for VPS29, n = 116 from seven cells for GalT).

(J) Western blotting confirming the knockdown of SNX2 in WT cells.

(K) Live confocal images showing presence of the PI4P probe GFP-$P4C_{SidC}$, GFP-PI4KIIα, and GFP-PI4KIIβ at the tips of actin tails in VAP DKO cells. Scale bar, 2 μm. See also Movie S7.

(L and M) Loss of assembled actin (phalloidin) and WASH immunofluorescence on intracellular organelles in VAP DKO cells upon PI4KIIs knockdown (L). Scale bar, 10 μm. Normalized fluorescence intensity of WASH and phalloidin on the region occupied by EEA1-positive endosomes (see Figure S7I) is quantified in (M) (n = 25 cells for either control or PI4KIIs siRNAs, two-tailed t test).

(N–P) Loss of PI4P on endosomal vesicles in PI4KIIs knockdown cells, as examined by two distinct PI4P probes, GFP-PH_{OSBP} and GFP-$P4C_{SidC}$ (N). Western blotting confirms the knockdown of PI4KIIα and PI4KIIβ in DKO cells (O). Quantification of the normalized fluorescence of GFP-$P4C_{SidC}$ is shown in (P) (WT n = 36 cells; DKO n = 40 cells for control siRNA, and n = 50 for PI4KIIs siRNA, two-tailed t test).

(Q) Schematic illustration of ER contacts that regulate WASH-dependent actin nucleation on endosomes and retromer-dependent budding by regulating PI4P. A pool of PI4P is synthesized on endosomes by type II PI4Ks. VAP, an ER protein that forms dimers and oligomers, contributes to ER-endosome tethers via its binding to the retromer subunit SNX2 and to OSBP, which binds PI4P on the endosomal membrane via its PH domain. OSBP, via its ORD domain, makes PI4P accessible to the ER-anchored inositol 4-phosphatase Sac1. In WT cells, a transient accumulation of PI4P on endosomes is coupled to a transient burst of WASH-dependent actin nucleation to facilitate retromer function. In cells that lack VAP, loss of PI4P downregulation results in excessive and persistent PI4P accumulation and actin nucleation on endosomes and in disruption of retromer-dependent budding.

hybrid endosome-*trans*-Golgi vesicles. The occurrence of actin comets indicates a persistent nucleation of actin with a loss of the mechanism(s) that normally terminate(s) this process. Downregulation of PI4P and fission of retromer-dependent tubules could be the events leading to termination of actin assembly in WT cells.

An exaggerated actin nucleation is reminiscent of what has been observed upon inhibition of fission at endocytic sites, where actin nucleation is promoted by N-WASP in a PI(4,5)P_2-dependent way (Merrifield and Kaksonen, 2014; Ferguson et al., 2009; Messa et al., 2014). PI4P may have an equivalent role in actin nucleation promoted by WASH. KD of type II PI 4-kinases in VAP DKO cells impaired the association of WASH with endosomes and actin comet formation. Conversely, KD of OSBP in WT cells resulted in the elevation of PI4P on intracellular vesicles and in WASH-dependent actin comets formation. Further supporting a role of PI4P in WASH dynamics, the WASH complex was reported to interact with type II PI 4-kinase (Ryder et al., 2013), and a genetic interaction was observed between the single *Drosophila* type II PI 4-kinase and the retromer (Burgess et al., 2012). Additionally, KD of PI4KIIα in mammalian cells impairs endosome traffic (Minogue et al., 2006). Surprisingly, inhibition of PI3P synthesis on endosomes enhanced WASH recruitment and actin nucleation. Possibly, PI4P is confined to endosomal microdomains in WT cells, and loss of PI3P disrupts this segregation allowing the PI4P domain to expand. As PI3P is required for retromer assembly at the endosomal surface, we suggest a hand-over mechanism from PI3P- to PI4P-dependent interactions in retromer/WASH-dependent budding. The robust WASH-dependent actin nucleation on endosomes upon loss of PI3P clearly indicates that WASH can function in actin nucleation independently of the retromer.

Recently, Rowland et al. (2014) showed that a large fraction of retromer-dependent tubular buds on endosomes undergo fission at sites where they are closely apposed to the ER and that are marked by the presence of FAM21, the linker between the retromer and WASH. VAP may be a component of ER-endosomes tethers at these sites and may impact the fission reaction via the recruitment of OSBP and PI4P downregulation. Focal accumulation of VAP at retromer positive sites can be detected only if SNX2 is overexpressed. However, in WT cells a transient interaction of ER with endosomes involving endogenous retromer and endogenous VAP may have a physiological effect without resulting in a major accumulation of VAP.

In conclusion, the new insight into VAP function provided by this study advances our knowledge of mechanisms that control PI4P dynamics and membrane traffic at the endosome-Golgi complex interface and the role of PI4P in this regulation. This insight may be useful to understand mechanisms through which VAP mutations lead to disease. Mutations in subunits of the WASH complex (strumpellin) and of the retromer (VPS35), i.e., two complexes which, as our results show, have interrelated functions downstream of VAP, have been implicated in neurodegenerative diseases, including Alzheimer's and Parkinson's (Small and Petsko, 2015; Valdmanis et al., 2007). Most interestingly, the VPS35 Parkinson mutation impairs its binding to WASH (Zavodszky et al., 2014). Further elucidation of the proteins network discussed here may help shed new light on pathogenetic mechanisms in these diseases.

EXPERIMENTAL PROCEDURES

An overview of experimental procedures is provided below. See the Supplemental Experimental Procedures for details.

Generation of VAP Knockout Cells with TALENs

Editing of gene targeting (disruption of exon 2) was validated by the Surveyor Nuclease assay. Gene-edited cells were enriched by fluorescence-based cell sorting using the surrogate reporter as published (Kim et al., 2011). Individual clones were isolated by limiting dilution and verification of targeted gene disruption was performed by PCR genotyping and sequencing.

Fluorescence Microscopy

For immunofluorescence, cells were grown on glass coverslips (Neuvitro), fixed with 4% paraformaldehyde (PFA) and then processed by standard procedures. To monitor CI-MPR internalization, cells were incubated at 37°C in serum-free DMEM containing 10 μg/ml mouse anti-CI-MPR monoclonal antibody (mAb) for up to 60 min, quickly rinsed with PBS, and then immunostained for the internalized antibodies. Imaging was performed by spinning disc confocal (SDC) microscopy, unless otherwise specified.

For live cell imaging, cells were plated on 35-mm glass bottom dishes (MatTek Corp) at low density, allowed to attach overnight, transfected, and imaged with a SDC microscope 16–20 hr after transfection. Spinning disc confocal (SDC) microscopy was performed as described in the Supplemental Experimental Procedures.

Phosphoinositide Analysis

WT and VAP DKO cells at similar confluency on 10-cm dishes were metabolically labeled with [^{3}H]myo-inositol (MP Biomedicals) in inositol-free DMEM (MP Biomedicals) for 48 hr. Subsequently, lipids were extracted, deacylated and [^{3}H]-labeled glycerophosphoinositol moieties were separated using high performance liquid chromatography (Shimadzu Scientific Instruments) and detected by an online flow scintillation analyzer (B-RAM, IN/US).

SUPPLEMENTAL INFORMATION

Supplemental Information includes Supplemental Experimental Procedures, seven figures, and seven movies and can be found with this article online at http://dx.doi.org/10.1016/j.cell.2016.06.037.

AUTHOR CONTRIBUTIONS

All authors contributed to some aspects of experimental design and data analysis. R.D. and Y.S. generated genome-edited cells. HPLC-based lipid analysis was performed by L.L. and mass spectrometry by S.S. and J.W.H. All other experiments were performed by R.D. who also had the major role in the development of the project. R.D. and P.D.C. wrote the manuscript.

ACKNOWLEDGMENTS

We thank Christopher Burd, Shawn Ferguson, and Jeeyun Chung for reading of the manuscript and discussion, Tim Levine (UCL, London) for sharing information about the FFAT consensus prior to its publication, and Cameron Godecke (Yale Cell Sorting Core Facility) for help in cell sorting. This work was supported in part by grants from the NIH (R37NS036251, DK45735, DA018343 and DK082700 to P.D.C. and R37NS083524 to J.W.H.), by the Harvard Brain Institute ALS Seed Grant Program to J.W.H., by the Biogen Idec ALS consortium to P.D.C. and J.W.H., by a CSC-Yale World Scholars Program scholarship to R.D., a postdoctoral fellowship from the Japan Society for the Promotion of Science to Y.S., and by a post-doctoral fellowship from Canadian Institutes for Health Research to S.S.

Received: August 13, 2015
Revised: April 15, 2016
Accepted: June 17, 2016
Published: July 14, 2016

REFERENCES

Alpy, F., Rousseau, A., Schwab, Y., Legueux, F., Stoll, I., Wendling, C., Spiegelhalter, C., Kessler, P., Mathelin, C., Rio, M.-C., et al. (2013). STARD3 or STARD3NL and VAP form a novel molecular tether between late endosomes and the ER. J. Cell Sci. *126*, 5500–5512.

Bago, R., Malik, N., Munson, M.J., Prescott, A.R., Davies, P., Sommer, E., Shpiro, N., Ward, R., Cross, D., Ganley, I.G., and Alessi, D.R. (2014). Characterization of VPS34-IN1, a selective inhibitor of Vps34, reveals that the phosphatidylinositol 3-phosphate-binding SGK3 protein kinase is a downstream target of class III phosphoinositide 3-kinase. Biochem. J. *463*, 413–427.

Balla, A., Tuymetova, G., Barshishat, M., Geiszt, M., and Balla, T. (2002). Characterization of type II phosphatidylinositol 4-kinase isoforms reveals association of the enzymes with endosomal vesicular compartments. J. Biol. Chem. *277*, 20041–20050.

Bojjireddy, N., Botyanszki, J., Hammond, G., Creech, D., Peterson, R., Kemp, D.C., Snead, M., Brown, R., Morrison, A., Wilson, S., et al. (2014). Pharmacological and genetic targeting of the PI4KA enzyme reveals its important role in maintaining plasma membrane phosphatidylinositol 4-phosphate and phosphatidylinositol 4,5-bisphosphate levels. J. Biol. Chem. *289*, 6120–6132.

Bonifacino, J.S., and Rojas, R. (2006). Retrograde transport from endosomes to the trans-Golgi network. Nat. Rev. Mol. Cell Biol. *7*, 568–579.

Burd, C., and Cullen, P.J. (2014). Retromer: a master conductor of endosome sorting. Cold Spring Harb. Perspect. Biol. *6*, a016774.

Burgess, J., Del Bel, L.M., Ma, C.-I.J., Barylko, B., Polevoy, G., Rollins, J., Albanesi, J.P., Krämer, H., and Brill, J.A. (2012). Type II phosphatidylinositol 4-kinase regulates trafficking of secretory granule proteins in Drosophila. Development *139*, 3040–3050.

Chung, J., Torta, F., Masai, K., Lucast, L., Czapla, H., Tanner, L.B., Narayanaswamy, P., Wenk, M.R., Nakatsu, F., and De Camilli, P. (2015). Intracellular transport. PI4P/phosphatidylserine countertransport at ORP5- and ORP8-mediated ER-plasma membrane contacts. Science *349*, 428–432.

Cole, N.B., Smith, C.L., Sciaky, N., Terasaki, M., Edidin, M., and Lippincott-Schwartz, J. (1996). Diffusional mobility of Golgi proteins in membranes of living cells. Science *273*, 797–801.

Dawson, P.A., Ridgway, N.D., Slaughter, C.A., Brown, M.S., and Goldstein, J.L. (1989). cDNA cloning and expression of oxysterol-binding protein, an oligomer with a potential leucine zipper. J. Biol. Chem. *264*, 16798–16803.

de Saint-Jean, M., Delfosse, V., Douguet, D., Chicanne, G., Payrastre, B., Bourguet, W., Antonny, B., and Drin, G. (2011). Osh4p exchanges sterols for phosphatidylinositol 4-phosphate between lipid bilayers. J. Cell Biol. *195*, 965–978.

Derivery, E., Sousa, C., Gautier, J.J., Lombard, B., Loew, D., and Gautreau, A. (2009). The Arp2/3 activator WASH controls the fission of endosomes through a large multiprotein complex. Dev. Cell *17*, 712–723.

Di Paolo, G., Pellegrini, L., Letinic, K., Cestra, G., Zoncu, R., Voronov, S., Chang, S., Guo, J., Wenk, M.R., and De Camilli, P. (2002). Recruitment and regulation of phosphatidylinositol phosphate kinase type 1 gamma by the FERM domain of talin. Nature *420*, 85–89.

Dickson, E.J., Jensen, J.B., Vivas, O., Kruse, M., Traynor-Kaplan, A.E., and Hille, B. (2016). Dynamic formation of ER-PM junctions presents a lipid phosphatase to regulate phosphoinositides. J. Cell Biol. *213*, 33–48.

Doughman, R.L., Firestone, A.J., and Anderson, R.A. (2003). Phosphatidylinositol phosphate kinases put PI4,5P(2) in its place. J. Membr. Biol. *194*, 77–89.

Ferguson, S.M., Raimondi, A., Paradise, S., Shen, H., Mesaki, K., Ferguson, A., Destaing, O., Ko, G., Takasaki, J., Cremona, O., et al. (2009). Coordinated actions of actin and BAR proteins upstream of dynamin at endocytic clathrin-coated pits. Dev. Cell *17*, 811–822.

Giordano, F., Saheki, Y., Idevall-Hagren, O., Colombo, S.F., Pirruccello, M., Milosevic, I., Gracheva, E.O., Bagriantsev, S.N., Borgese, N., and De Camilli, P. (2013). PI(4,5)P_2-dependent and Ca(2+)-regulated ER-PM interactions mediated by the extended synaptotagmins. Cell *153*, 1494–1509.

Godi, A., Pertile, P., Meyers, R., Marra, P., Di Tullio, G., Iurisci, C., Luini, A., Corda, D., and De Matteis, M.A. (1999). ARF mediates recruitment of PtdIns-4-OH kinase-beta and stimulates synthesis of PtdIns(4,5)P2 on the Golgi complex. Nat. Cell Biol. *1*, 280–287.

Gomez, T.S., and Billadeau, D.D. (2009). A FAM21-containing WASH complex regulates retromer-dependent sorting. Dev. Cell *17*, 699–711.

Hammond, G.R.V., and Balla, T. (2015). Polyphosphoinositide binding domains: key to inositol lipid biology. Biochim. Biophys. Acta *1851*, 746–758.

Harbour, M.E., Breusegem, S.Y., and Seaman, M.N.J. (2012). Recruitment of the endosomal WASH complex is mediated by the extended 'tail' of Fam21 binding to the retromer protein Vps35. Biochem. J. *442*, 209–220.

Henmi, Y., Morikawa, Y., Oe, N., Ikeda, N., Fujita, A., Takei, K., Minogue, S., and Tanabe, K. (2016). PtdIns4KIIα generates endosomal PtdIns(4)P and is required for receptor sorting at early endosomes. Mol. Biol. Cell *27*, 990–1001.

Hierro, A., Rojas, A.L., Rojas, R., Murthy, N., Effantin, G., Kajava, A.V., Steven, A.C., Bonifacino, J.S., and Hurley, J.H. (2007). Functional architecture of the retromer cargo-recognition complex. Nature *449*, 1063–1067.

Holthuis, J.C.M., and Menon, A.K. (2014). Lipid landscapes and pipelines in membrane homeostasis. Nature *510*, 48–57.

Huttlin, E.L., Ting, L., Bruckner, R.J., Gebreab, F., Gygi, M.P., Szpyt, J., Tam, S., Zarraga, G., Colby, G., Baltier, K., et al. (2015). The BioPlex Network: a systematic exploration of the human interactome. Cell *162*, 425–440.

Im, Y.J., Raychaudhuri, S., Prinz, W.A., and Hurley, J.H. (2005). Structural mechanism for sterol sensing and transport by OSBP-related proteins. Nature *437*, 154–158.

Kabashi, E., El Oussini, H., Bercier, V., Gros-Louis, F., Valdmanis, P.N., McDearmid, J., Mejier, I.A., Dion, P.A., Dupre, N., Hollinger, D., et al. (2013). Investigating the contribution of VAPB/ALS8 loss of function in amyotrophic lateral sclerosis. Hum. Mol. Genet. *22*, 2350–2360.

Kaiser, S.E., Brickner, J.H., Reilein, A.R., Fenn, T.D., Walter, P., and Brunger, A.T. (2005). Structural basis of FFAT motif-mediated ER targeting. Structure *13*, 1035–1045.

Kim, S., Leal, S.S., Ben Halevy, D., Gomes, C.M., and Lev, S. (2010). Structural requirements for VAP-B oligomerization and their implication in amyotrophic lateral sclerosis-associated VAP-B(P56S) neurotoxicity. J. Biol. Chem. *285*, 13839–13849.

Kim, H., Um, E., Cho, S.-R., Jung, C., Kim, H., and Kim, J.-S. (2011). Surrogate reporters for enrichment of cells with nuclease-induced mutations. Nat. Methods *8*, 941–943.

Knight, Z.A., Gonzalez, B., Feldman, M.E., Zunder, E.R., Goldenberg, D.D., Williams, O., Loewith, R., Stokoe, D., Balla, A., Toth, B., et al. (2006). A pharmacological map of the PI3-K family defines a role for p110alpha in insulin signaling. Cell *125*, 733–747.

Lahiri, S., Toulmay, A., and Prinz, W.A. (2015). Membrane contact sites, gateways for lipid homeostasis. Curr. Opin. Cell Biol. *33*, 82–87.

Levine, T., and Loewen, C. (2006). Inter-organelle membrane contact sites: through a glass, darkly. Curr. Opin. Cell Biol. *18*, 371–378.

Luo, X., Wasilko, D.J., Liu, Y., Sun, J., Wu, X., Luo, Z.-Q., and Mao, Y. (2015). Structure of the Legionella virulence factor, SidC reveals a unique PI(4)P-specific binding domain essential for its targeting to the bacterial phagosome. PLoS Pathog. *11*, e1004965.

Maeda, K., Anand, K., Chiapparino, A., Kumar, A., Poletto, M., Kaksonen, M., and Gavin, A.-C. (2013). Interactome map uncovers phosphatidylserine transport by oxysterol-binding proteins. Nature *501*, 257–261.

Manford, A.G., Stefan, C.J., Yuan, H.L., Macgurn, J.A., and Emr, S.D. (2012). ER-to-plasma membrane tethering proteins regulate cell signaling and ER morphology. Dev. Cell *23*, 1129–1140.

Merrifield, C.J., and Kaksonen, M. (2014). Endocytic accessory factors and regulation of clathrin-mediated endocytosis. Cold Spring Harb. Perspect. Biol. *6*, a016733.

Mesmin, B., Bigay, J., Moser von Filseck, J., Lacas-Gervais, S., Drin, G., and Antonny, B. (2013). A four-step cycle driven by PI(4)P hydrolysis directs sterol/PI(4)P exchange by the ER-Golgi tether OSBP. Cell *155*, 830–843.

Messa, M., Fernández-Busnadiego, R., Sun, E.W., Chen, H., Czapla, H., Wrasman, K., Wu, Y., Ko, G., Ross, T., Wendland, B., and De Camilli, P. (2014). Epsin deficiency impairs endocytosis by stalling the actin-dependent invagination of endocytic clathrin-coated pits. eLife *3*, e03311.

Minogue, S., Waugh, M.G., De Matteis, M.A., Stephens, D.J., Berditchevski, F., and Hsuan, J.J. (2006). Phosphatidylinositol 4-kinase is required for endosomal trafficking and degradation of the EGF receptor. J. Cell Sci. *119*, 571–581.

Moser von Filseck, J., Čopič, A., Delfosse, V., Vanni, S., Jackson, C.L., Bourguet, W., and Drin, G. (2015). Intracellular transport. Phosphatidylserine transport by ORP/Osh proteins is driven by phosphatidylinositol 4-phosphate. Science *349*, 432–436.

Murphy, S.E., and Levine, T.P. (2016). VAP, a Versatile Access Point for the Endoplasmic Reticulum: Review and analysis of FFAT-like motifs in the VAPome. Biochim. Biophys. Acta *1861* (8 Pt B), 952–961.

Nakatsu, F., Baskin, J.M., Chung, J., Tanner, L.B., Shui, G., Lee, S.Y., Pirruccello, M., Hao, M., Ingolia, N.T., Wenk, M.R., and De Camilli, P. (2012). PtdIns4P synthesis by PI4KIIIα at the plasma membrane and its impact on plasma membrane identity. J. Cell Biol. *199*, 1003–1016.

Nandez, R., Balkin, D.M., Messa, M., Liang, L., Paradise, S., Czapla, H., Hein, M.Y., Duncan, J.S., Mann, M., and De Camilli, P. (2014). A role of OCRL in clathrin-coated pit dynamics and uncoating revealed by studies of Lowe syndrome cells. Elife *3*, e02975.

Nishimura, A.L., Mitne-Neto, M., Silva, H.C.A., Richieri-Costa, A., Middleton, S., Cascio, D., Kok, F., Oliveira, J.R.M., Gillingwater, T., Webb, J., et al. (2004). A mutation in the vesicle-trafficking protein VAPB causes late-onset spinal muscular atrophy and amyotrophic lateral sclerosis. Am. J. Hum. Genet. *75*, 822–831.

Olkkonen, V.M., and Levine, T.P. (2004). Oxysterol binding proteins: in more than one place at one time? Biochem. Cell Biol. *82*, 87–98.

Papiani, G., Ruggiano, A., Fossati, M., Raimondi, A., Bertoni, G., Francolini, M., Benfante, R., Navone, F., and Borgese, N. (2012). Restructured endoplasmic reticulum generated by mutant amyotrophic lateral sclerosis-linked VAPB is cleared by the proteasome. J. Cell Sci. *125*, 3601–3611.

Peretti, D., Dahan, N., Shimoni, E., Hirschberg, K., and Lev, S. (2008). Coordinated lipid transfer between the endoplasmic reticulum and the Golgi complex requires the VAP proteins and is essential for Golgi-mediated transport. Mol. Biol. Cell *19*, 3871–3884.

Puthenveedu, M.A., Lauffer, B., Temkin, P., Vistein, R., Carlton, P., Thorn, K., Taunton, J., Weiner, O.D., Parton, R.G., and von Zastrow, M. (2010). Sequence-dependent sorting of recycling proteins by actin-stabilized endosomal microdomains. Cell *143*, 761–773.

Raiborg, C., Wenzel, E.M., Pedersen, N.M., Olsvik, H., Schink, K.O., Schultz, S.W., Vietri, M., Nisi, V., Bucci, C., Brech, A., et al. (2015). Repeated ER-endosome contacts promote endosome translocation and neurite outgrowth. Nature *520*, 234–238.

Rocha, N., Kuijl, C., van der Kant, R., Janssen, L., Houben, D., Janssen, H., Zwart, W., and Neefjes, J. (2009). Cholesterol sensor ORP1L contacts the ER protein VAP to control Rab7-RILP-p150 Glued and late endosome positioning. J. Cell Biol. *185*, 1209–1225.

Rowland, A.A., Chitwood, P.J., Phillips, M.J., and Voeltz, G.K. (2014). ER contact sites define the position and timing of endosome fission. Cell *159*, 1027–1041.

Rozelle, A.L., Machesky, L.M., Yamamoto, M., Driessens, M.H., Insall, R.H., Roth, M.G., Luby-Phelps, K., Marriott, G., Hall, A., and Yin, H.L. (2000). Phosphatidylinositol 4,5-bisphosphate induces actin-based movement of raft-enriched vesicles through WASP-Arp2/3. Curr. Biol. *10*, 311–320.

Ryder, P.V., Vistein, R., Gokhale, A., Seaman, M.N., Puthenveedu, M.A., and Faundez, V. (2013). The WASH complex, an endosomal Arp2/3 activator, interacts with the Hermansky-Pudlak syndrome complex BLOC-1 and its cargo phosphatidylinositol-4-kinase type IIα. Mol. Biol. Cell *24*, 2269–2284.

Saheki, Y., Bian, X., Schauder, C.M., Sawaki, Y., Surma, M.A., Klose, C., Pincet, F., Reinisch, K.M., and De Camilli, P. (2016). Control of plasma membrane lipid homeostasis by the extended synaptotagmins. Nat. Cell Biol. *18*, 504–515.

Sanjana, N.E., Cong, L., Zhou, Y., Cunniff, M.M., Feng, G., and Zhang, F. (2012). A transcription activator-like effector toolbox for genome engineering. Nat. Protoc. *7*, 171–192.

Schaub, B.E., Berger, B., Berger, E.G., and Rohrer, J. (2006). Transition of galactosyltransferase 1 from trans-Golgi cisterna to the trans-Golgi network is signal mediated. Mol. Biol. Cell *17*, 5153–5162.

Seaman, M.N., McCaffery, J.M., and Emr, S.D. (1998). A membrane coat complex essential for endosome-to-Golgi retrograde transport in yeast. J. Cell Biol. *142*, 665–681.

Small, S.A., and Petsko, G.A. (2015). Retromer in Alzheimer disease, Parkinson disease and other neurological disorders. Nat. Rev. Neurosci. *16*, 126–132.

Stefan, C.J., Manford, A.G., Baird, D., Yamada-Hanff, J., Mao, Y., and Emr, S.D. (2011). Osh proteins regulate phosphoinositide metabolism at ER-plasma membrane contact sites. Cell *144*, 389–401.

Teuling, E., Ahmed, S., Haasdijk, E., Demmers, J., Steinmetz, M.O., Akhmanova, A., Jaarsma, D., and Hoogenraad, C.C. (2007). Motor neuron disease-associated mutant vesicle-associated membrane protein-associated protein (VAP) B recruits wild-type VAPs into endoplasmic reticulum-derived tubular aggregates. J. Neurosci. *27*, 9801–9815.

Valdmanis, P.N., Meijer, I.A., Reynolds, A., Lei, A., MacLeod, P., Schlesinger, D., Zatz, M., Reid, E., Dion, P.A., Drapeau, P., and Rouleau, G.A. (2007). Mutations in the KIAA0196 gene at the SPG8 locus cause hereditary spastic paraplegia. Am. J. Hum. Genet. *80*, 152–161.

Willars, G.B., Nahorski, S.R., and Challiss, R.A. (1998). Differential regulation of muscarinic acetylcholine receptor-sensitive polyphosphoinositide pools and consequences for signaling in human neuroblastoma cells. J. Biol. Chem. *273*, 5037–5046.

Zavodszky, E., Seaman, M.N.J., Moreau, K., Jimenez-Sanchez, M., Breusegem, S.Y., Harbour, M.E., and Rubinsztein, D.C. (2014). Mutation in VPS35 associated with Parkinson's disease impairs WASH complex association and inhibits autophagy. Nat. Commun. *5*, 3828.

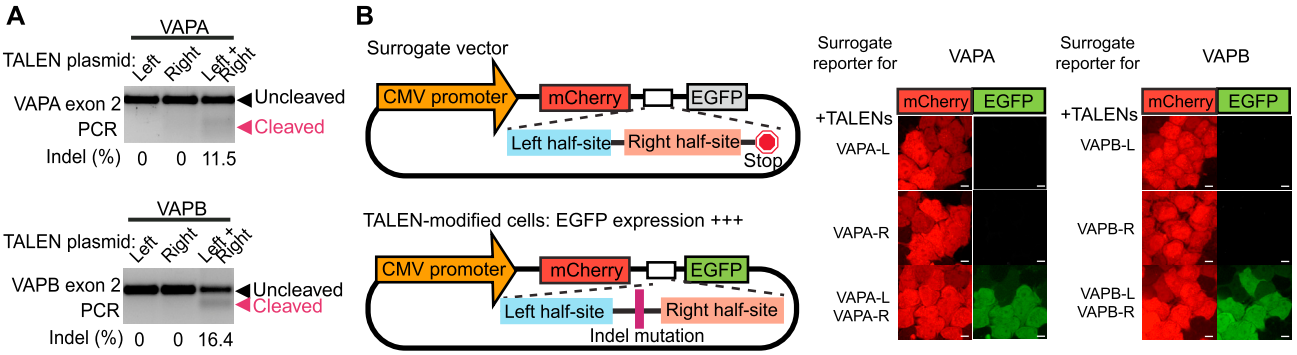

C

	VAPA		VAPB	
WT	TAGTCACTACAAATCTTAAATTGCGAAATCCATCGGATAGAAAAGTGTGTTTCAAAGTGA		TTTTAAGGTGAAGACTACAGCACCACGTAGGTACTGTGTGAGGCCCAACAGCGGAATCA	
DKO_1	Deletion of the entire exon2 in mRNA		TTTTAAGGTGAAGACTACAGCACCA----------ACAGCGGAATCA TTTTAAGGTGAAGACTACAGCACCA---AGGT-CTGTGTGAGGCCCAACAGCGGAATCA	Δ 22 Δ 4
DKO_2	TAGTCACTACAAATCTTAAATTGCGAAAT----CGGATAGAAAAGTGTGTTTCAAAGTGA TAGTCACTACAAATCTTAAATTGCGA----------TAGAAAAGTGTGTTTCAAAGTGA	Δ 4 Δ 11	TTTTAAGGTGAAGACTACAGCACCACG----TACTGTGTGAGGCCCAACAGCGGAATCA TTTTAAGGTGAAGACTACAGCACCAC--------TGTGTGAGGCCCAACAGCGGAATCA	Δ 4 Δ 8
DKO_3	TAGTCACTACAAATCTTAAATTGCGAAAT----CGGATAGAAAAGTGTGTTTCAAAGTGA TAGTCACTACAAATCTTAAATTGCGA----------TAGAAAAGTGTGTTTCAAAGTGA	Δ 4 Δ 11	TTTTAAGGTGAAGACTACAGCACCACGTAG-------GTGAGGCCCAACAGCGGAATCA TTTTAAGGTGAAGACTACAGCA----------TGTGAGGCCCAACAGCGGAATCA	Δ 7 Δ 14

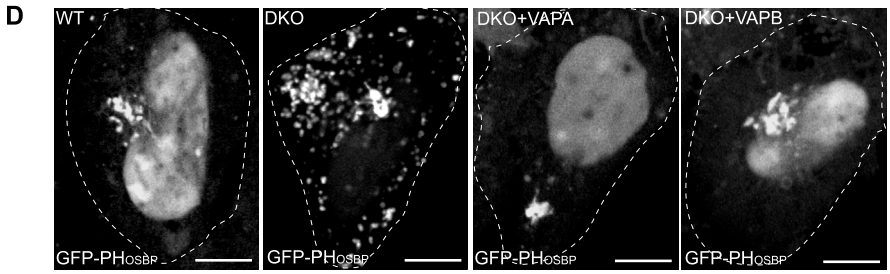

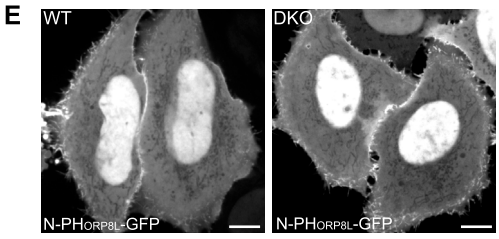

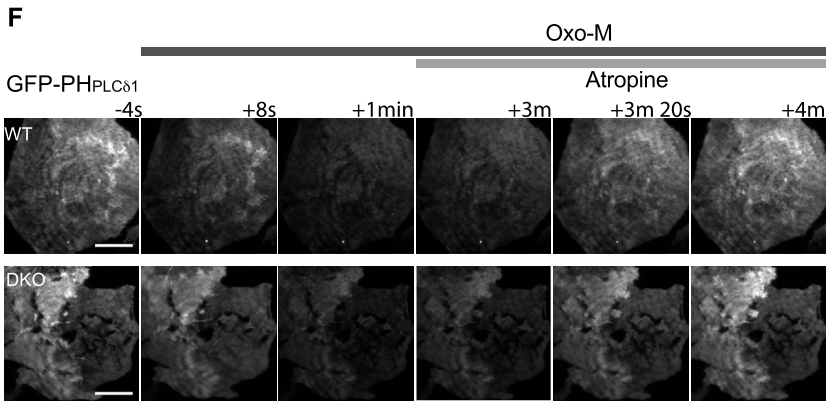

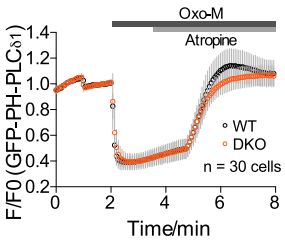

(legend on next page)

Figure S1. Increased Abundance of PI4P on Endosomes of VAP DKO Cells, Related to Figure 1

(A) Surveyor nuclease assay for TALEN-induced DNA cleavage in VAPA and VAPB loci. Wild-type HeLa cells were transfected with plasmids expressing VAPA or VAPB TALEN pairs and incubated for 72 hr before genomic DNA extraction. ~500 bp fragments around each target site were PCR amplified and analyzed for targeted DNA cleavage efficiency by the Surveyor nuclease assay.

(B) Left: schematic illustration of the surrogate reporter system used to facilitate enrichment of TALEN-modified cells. The surrogate vector, encodes mCherry and EFGP separated by a DNA stretch that includes the sequence targeted by TALEN followed by a stop codon. TALEN-dependent editing places the STOP codon out of frames leading to a mCherry-EGFP fusion protein. Right: fluorescence of cells transfected with both the TALENs (left TALEN, right TALEN or the TALEN pair as indicated) and the surrogate reporter. The presence of both red and green fluorescence on a subset of cells validated effectiveness of TALEN-dependent gene recombination.

(C) Genomic sequence of the regions of VAPA and VAPB exon 2 targeted by the VAP TALEN pairs. Nucleotides in red and blue indicate the binding regions of left and right arm of the TALEN pair respectively. WT: sequence of the WT loci. DKO-1, 2 and 3: edited sequences in the three VAP double knockout HeLa cell lines (DKO) used in this study with the number of deleted (Δ) nucleotides shown at right in black. With the exception of the mutation of the VAPA locus in DKO-1, which results in the complete deletion of exon 2, all other mutations cause frame-shifts. In all cases, the result is the ablation of VAPA and VAPB protein expression.

(D) Confocal images of WT and VAP DKO cells expressing the PI4P probe GFP-PH_{OSBP} and showing the robust accumulation of this probe on intracellular vesicular compartments in VAP DKO cells. This accumulation is rescued by the co-expression of HA-VAPA or Myc-VAPB. The probe is known to partially localize in the nucleus in WT cells (Balla et al., 2005), but such localization is lost upon increase of PI4P levels on cytoplasmic membranes. Scale bar, 10 μm.

(E) Confocal images of WT and VAP DKO cells expressing N-PH_{ORP8L}-EGFP, a low-affinity PI4P probe that labels selectively plasma membrane PI4P pools, showing that the plasma membrane level of PI4P is not obviously elevated in VAP DKO cells. The prominent nuclear localization of this probe is typically observed in WT cells and is lost when plasma membrane PI4P is elevated (see Figure 2L). Scale bar, 10 μm.

(F) TIRF images of wild-type and VAP DKO cells expressing the $PI(4,5)P_2$ marker GFP-$PH_{PLC\delta1}$ and M1R-mCherry. Cells were stimulated with Oxo-M (10 μM), followed by addition of atropine (an M1R receptor antagonist) (50 μM), as indicated. Scale bar, 10 μm.

(G) Time-course of normalized GFP fluorescence from the cells shown in (I) revealing no major changes in $PI(4,5)P_2$ dynamics in response to M1R stimulation in DKO cells. Data are represented as mean ± SEM (n = 30 cells for each genotype).

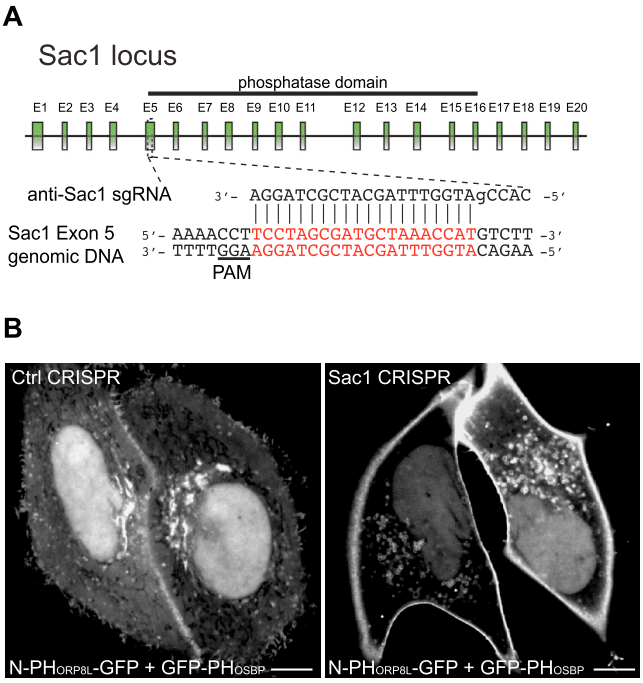

Figure S2. Depletion of Sac1 by CRISPR Results in PI4P Accumulation at Both Plasma Membrane and the Intracellular Vesicles, Related to Figure 2

(A) Schematic illustration of CRISPR targeting sites in exon 5 of the human Sac1 locus. Exon 5 encodes an amino acid stretch at the beginning of the phosphatase domain. The sequence targeted by the CRISPR is shown in red.

(B) Confocal images of WT and Sac1-CRISPR-treated cells co-expressing two different PI4P probes, N-PH_{ORP8L}-EGFP and GFP-PH_{OSBP}, which collectively label both plasma membrane (N-PH_{ORP8L}) and internal (GFP-PH_{OSBP}) PI4P pools. Note the increased GFP fluorescence at both the plasma membrane and intracellular vesicular compartments in Sac1-CRISPR-treated cells. Scale bar, 10 μm.

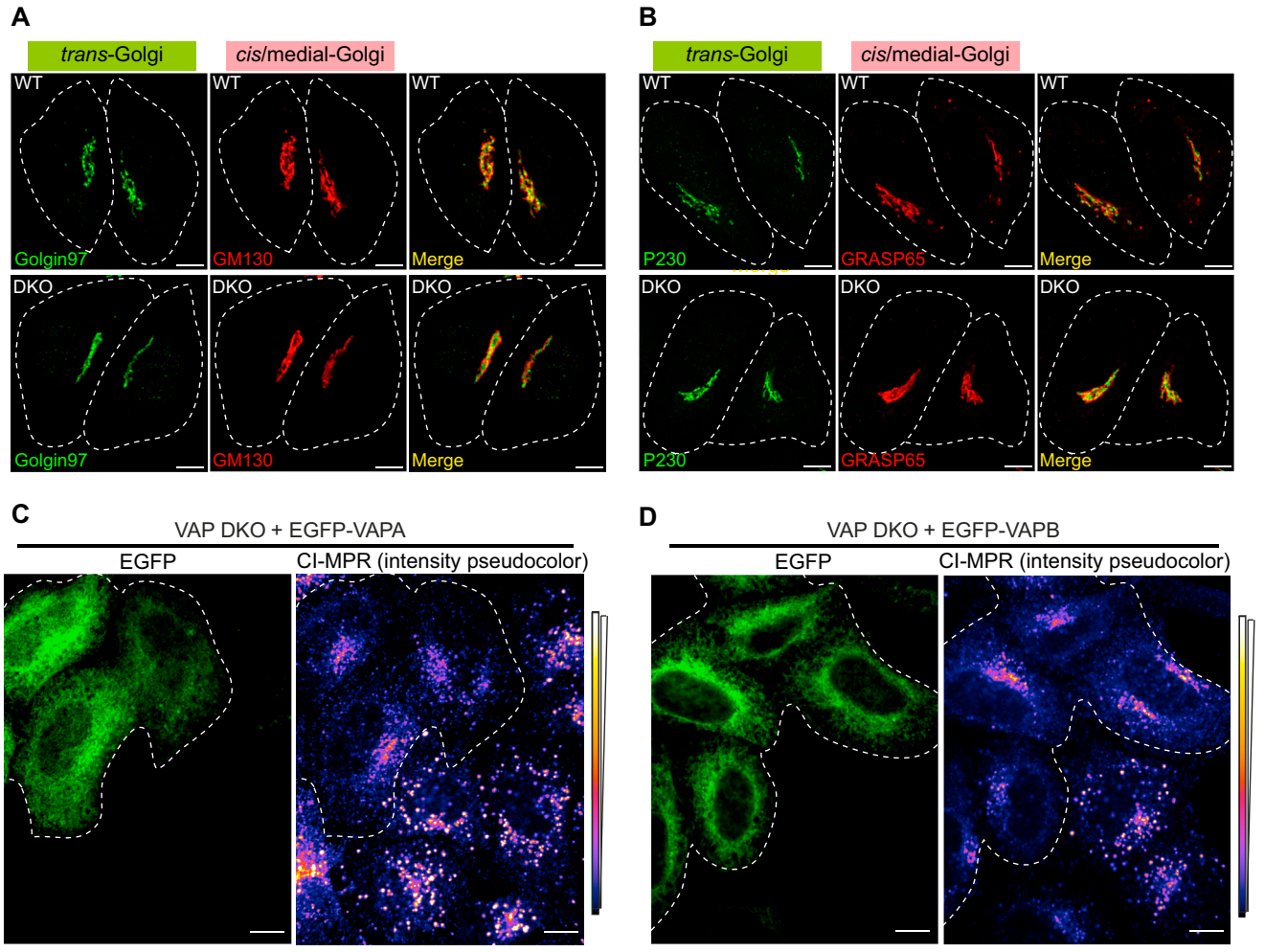

Figure S3. Defects in Retrograde Traffic from Endosomes to the Golgi Complex in VAP DKO Cells, Related to Figure 3

(A and B) Immunofluorescence against the indicated Golgi proteins in WT and VAP DKO cells, showing no obvious changes of the localization of these proteins in VAP DKO cells. Scale bar, 10 μm.

(C and D) Immunofluorescence images of internalized anti-CI-MPR antibody in VAP DKO cells expressing EGFP-VAPA (C) or EGFP-VAPB (D). The fluorescence signal was pseudocolored based on pixel intensity as indicated. In DKO cells not expressing EGFP-VAP, immunoreactivity has a dispersed punctate localization. The enrichment of the CI-MPR typically observed in the perinuclear region (corresponding to the TGN) of WT cells (see Figure 2H) was restored in DKO cells expressing GFP-tagged VAPs (cells enclosed by dashed lines). Scale bar, 10 μm.

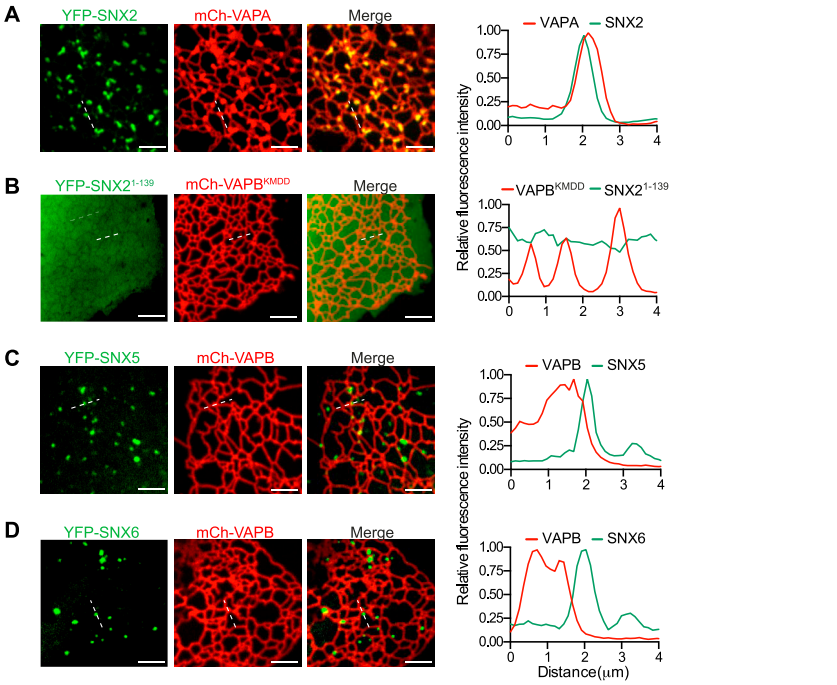

E

CompPASS analysis
HeLa: HA-VAPB+GFP-SNX2
Bait: VAPB (74 APSM)

HCIP	NWD-score	Z-score	APSM
SNX2	0.61	4.85	3
OSBP	0.61	4.85	3
OSBP2	1.22	5.07	3
OSBPL2	1.22	5.07	3
OSBPL3	0.32	4.78	5
OSBPL9	0.79	4.99	5
OSBPL10	0.71	4.96	4
OSBPL11	1.00	5.08	2
VAPA	1.77	5.10	16

F

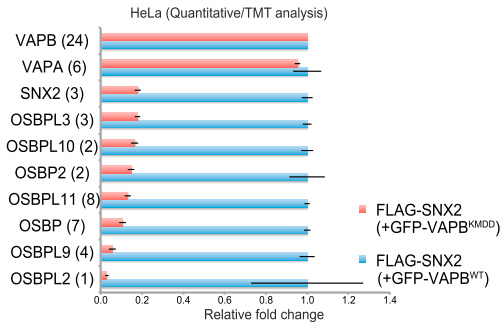

Figure S4. SNX2-VAPB Interaction, Related to Figure 4

(A–D) Fluorescence images of COS7 cells expressing the proteins as indicated. Double fluorescence images are at left and line scans at right. (A) Coclustering of YFP-SNX2 and mCherry-VAPA. (B) mCh-VAPB^{KMDD} (FFAT motif binding double mutant, *K87D M89D*) fails to recruit to the ER the C-terminally truncated SNX2 construct (YFP-SNX2$^{1-139}$). (C and D) Neither EGFP-SNX5 (C) nor EGFP-SNX6 (D), both of which have the typical punctate (endosomal) localization, cocluster with mCh-VAPB. Scale bar, 5 μm.

(E) Subset of VAPB high-confidence candidate interacting proteins (HCIPs) identified through CompPASS analysis (Sowa et al., 2009). Affinity purification mass spectrometry (AP-MS) of VAPB was performed from HeLa cells stably expressing HA-VAPB and GFP-SNX2. SNX2, VAPA, and several members of the OSBP family of proteins were identified as HCIPs of VAPB. Proteins with NWD-scores > 1.0 are considered HCIPs, although we also note that some proteins that may be bona fide interacting proteins may not reach the strict threshold set by a NWD-score of > 1.0. (APSM = Average Protein Spectral Matches, Normalized Weighted D-scores = NWD)

(F) Quantitative proteomics of WT and FFAT-binding deficient mutant VAPB (VAPB^{KMDD}). Quantitative/TMT proteomics performed from HeLa cell lines stably expressing GFP-SNX2 in the presence of either FLAG-VAPB^{WT} or FLAG-VAPB^{KMDD} demonstrating decreased interaction of VAPB^{KMDD} (relative to VAPB^{WT}) with SNX2 and members of the OSBP family, but not with VAPA. Relative intensities for VAPB^{WT} and VAPB^{KMDD} interacting proteins are shown. Error bars represent mean ± SE. Numbers of peptides quantified for each protein are listed in parentheses.

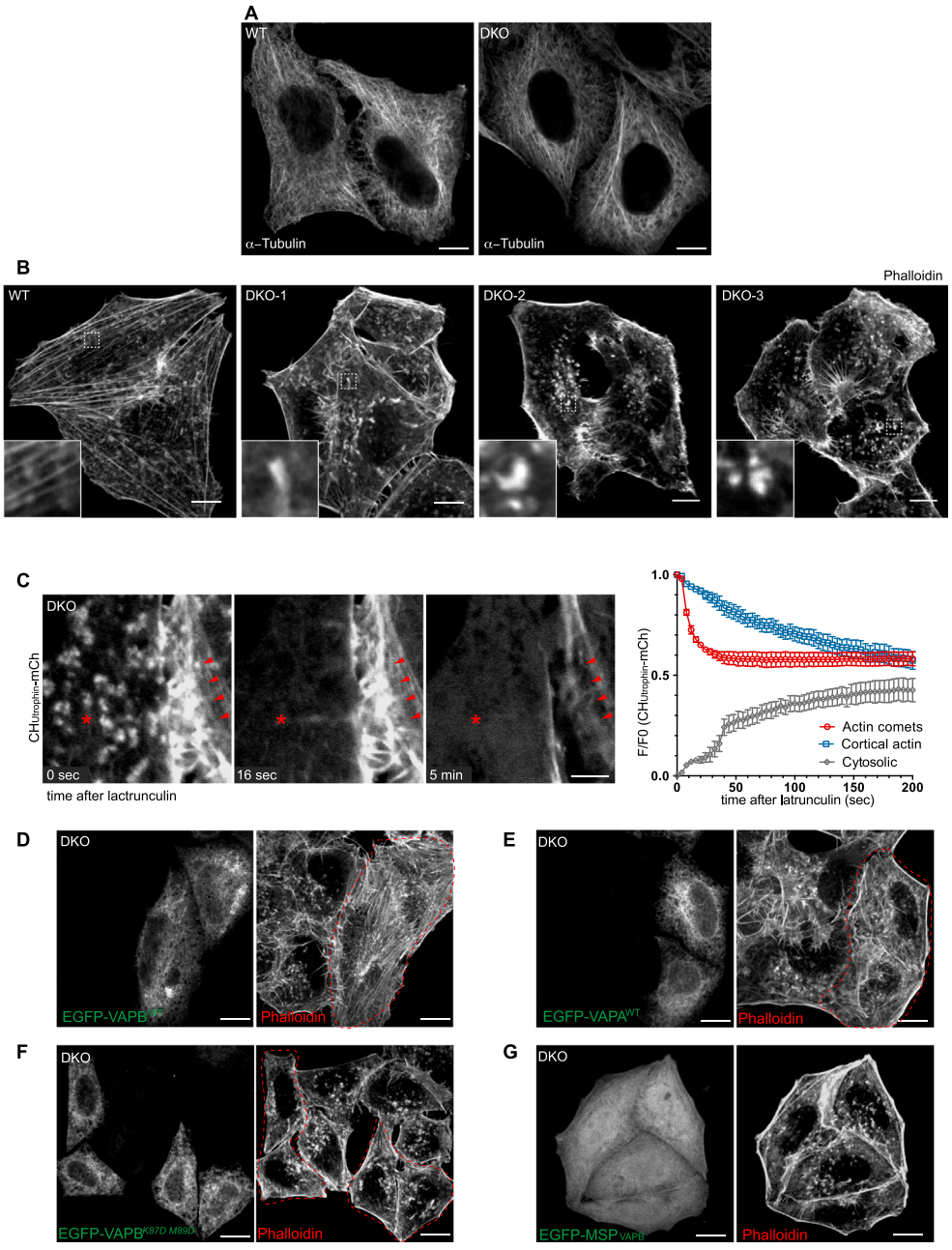

Figure S5. Massive Presence of Actin Comets in VAP DKO Cells, Related to Figure 5

(A) Immunofluorescence of α-tubulin in WT and VAP DKO cells showing that lack of VAP does not produce a major perturbation of the microtubular network. Scale bar, 10 μm.

(B) Phalloidin staining of WT and VAP DKO (three distinct clones) HeLa cells showing loss of actin stress fibers and accumulation of internal actin foci in VAP DKO cells. Most such foci have the appearance of actin comets (see insets). Scale bar, 10 μm.

(C) Confocal images of $CH_{Utrophin}$-mCh fluorescence from VAP DKO cells exposed to latrunculin B treatment (10 μM) for the indicated times, showing rapid loss of actin comets (asterisk) and slower loss of cortical actin (red arrowheads). Time course of the normalized mCherry fluorescence of actin comets, cortical actin, and cytosolic fluorescence after latrunculin B treatment is shown at right (n = 4 cells, error bars denote SEM).

(D and E) Phalloidin staining of VAP DKO cells expressing the EGFP-tagged wild-type VAPB or VAPA showing the rescue of the perturbation of the actin cytoskeleton in cells expressing either VAPB (D) or VAPA (E). Note the absence of internal actin foci (actin tails) and the abundance of stress fibers only in cells expressing VAP (cells surrounded by the red outline). Scale bar, 10 μm.

(F and G) Phalloidin staining of VAP DKO cells expressing the EGFP-tagged FFAT-motif binding deficient VAPB mutant (*K87D M89D*) (F), or the EGFP-tagged MSP domain-only of VAPB (G), showing that the actin foci (actin comets) of VAP DKO cells are not abolished by these VAP constructs. Scale bar, 10 μm.

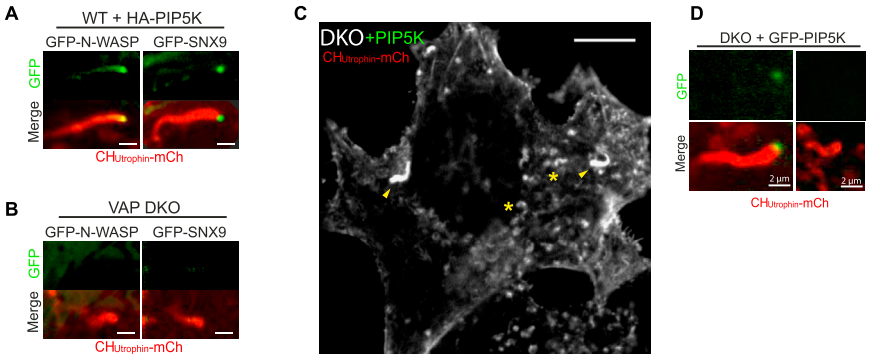

Figure S6. Actin Comets of VAP DKO Cells Are Not N-WASP-Dependent, Related to Figure 6

(A) Confocal images of actin comets from WT cells transfected with HA-tagged PIP5K1γ87 together with $CH_{Utrophin}$-mCh and either GFP-tagged N-WASP (left) or GFP-tagged SNX9 (right), showing that actin comets that form under these conditions (i.e., $PI(4,5)P_2$ overproduction as a result of PIP5K1γ87 overexpression) are positive for both N-WASP and SNX9 at their tips. Scale bar, 2 μm.

(B) Confocal images of actin comets in VAP DKO cells transfected with CH_{UTR}-mCh and GFP-tagged N-WASP or SNX9, as indicated, revealing that N-WASP and SNX9 were not associated with the actin comets resulting from the absence of VAP. Scale bar, 2 μm.

(C and D) (C) Fluorescence of $CH_{Utrophin}$-mCh in a VAP DKO cell also transfected with GFP-PIP5K1γ87. Note the presence of two large and long comet tails (arrowheads), clearly different from the majority of the other small tails (asterisks) typical of VAP DKO cells. As shown in (D), the thick and long tails, but not the small tails, are positive for GFP-PIP5K1γ87 at their tips, indicating their distinct nature. Scale bar: 2 μm.

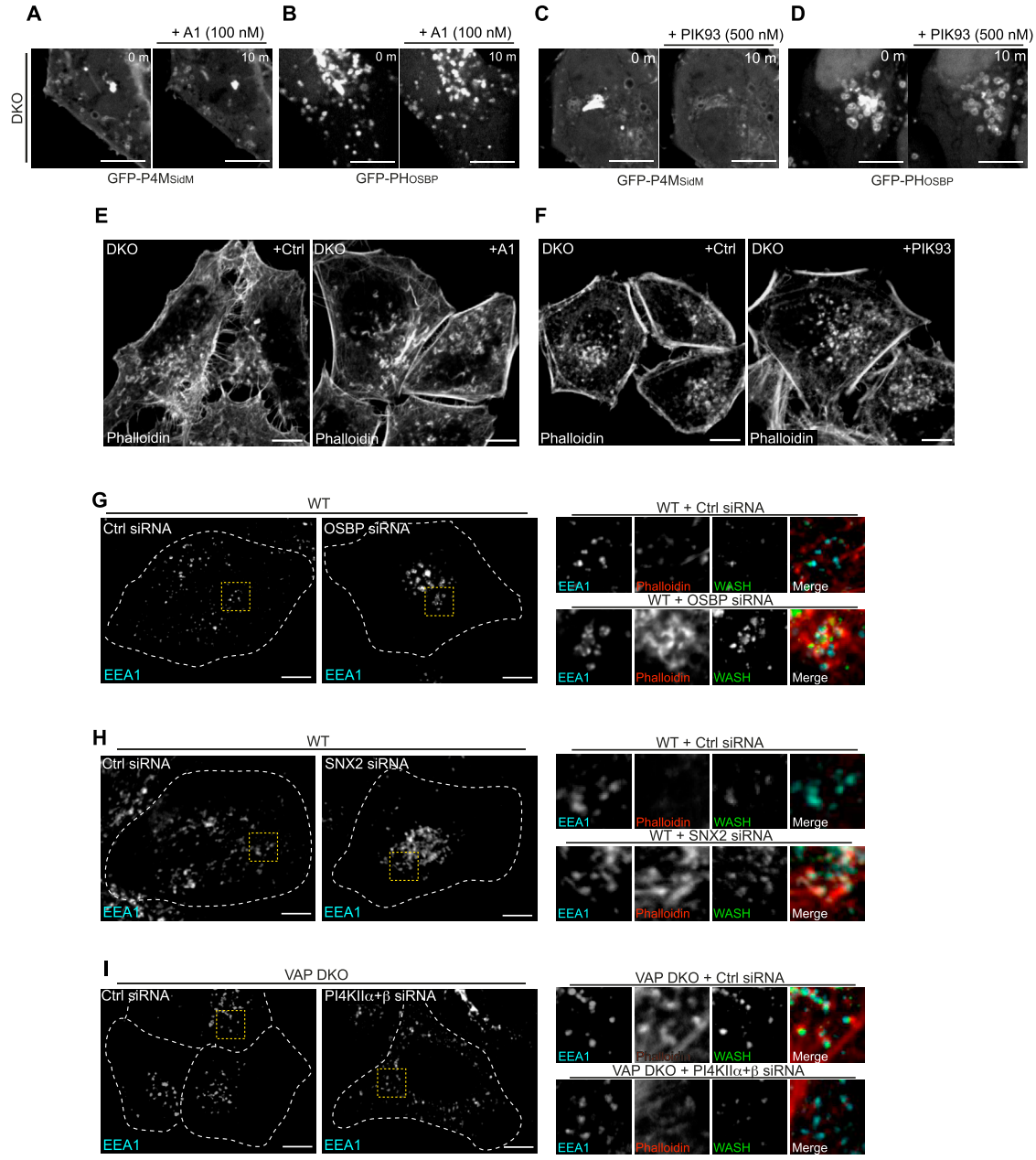

Figure S7. Impact of Pharmacological and Genetic Perturbation on the Nucleation of Actin on Intracellular Organelles, Related to Figure 7

(A–D) Confocal fluorescence images of VAP DKO cells expressing the PI4P probe P4M (A and C) or PH_{OSBP} (B and D) and treated for 10 min with the PI4KIIIα inhibitor A1 (100 nM) (A and B), or the PI4KIIIβ inhibitor PIK93 (500 nM) (C and D). The micrographs show that endosomal PI4P was not obviously affected by the inhibition of these two kinases that generate PI4P at the plasma membrane and the Golgi complex, respectively. Scale bar, 10 μm.

(E and F) Phalloidin staining of VAP DKO cells treated for 1h with the PI4KIIIα inhibitor A1 (100 nM) (E), or PI4KIIIβ inhibitor PIK93 (500 nM) (F), showing that these drugs do not affect actin comets. Scale bar, 10 μm.

(G–I) (Left) EEA1 immunofluorescence of WT (G, H) or VAP DKO (I) cells transfected with the indicated siRNAs. These micrographs correspond to the same cells shown in Figures 7A, 7F, and 7L, respectively, which were triple stained for phalloidin, WASH and EEA1. In Figure 7, the EEA1 immunofluorescence micrographs are not shown. They are shown here in order to indicate how the EEA1 fields were selected (see examples of the yellow squares with the corresponding EEA1, WASH and phalloidin staining at right) to provide the quantitative data shown in Figures 7B, 7G, and 7M. (Right) High-magnification of the regions enclosed by yellow dashed boxes, showing EEA1 and WASH immunoreactivities as well as phalloidin staining in these regions. Scale bar, 10 μm.

Cell, Volume *166*

Supplemental Information

Endosome-ER Contacts Control Actin Nucleation and Retromer Function through VAP-Dependent Regulation of PI4P

Rui Dong, Yasunori Saheki, Sharan Swarup, Louise Lucast, J. Wade Harper, and Pietro De Camilli

SUPPLEMENTAL MATERIALS FOR:

VAP-dependent ER-endosome contacts control WASH and retromer function through PI4P regulation

Rui Dong[1, 2, 3, 5], Yasunori Saheki[1, 2, 3, 5, 7], Sharan Swarup[6], Louise Lucast[1, 2, 3, 5], J. Wade Harper[6], Pietro De Camilli[1, 2, 3, 4, 5, *].

[1]Department of Neuroscience, Yale University School of Medicine, New Haven, Connecticut 06510, USA.
[2]Department of Cell Biology, Yale University School of Medicine, New Haven, CT 06510, USA.
[3]Howard Hughes Medical Institute, Yale University School of Medicine, New Haven, CT 06510, USA.
[4]Kavli Institute for Neurosciences, Yale University School of Medicine, New Haven, CT 06510, USA.
[5]Program in Cellular Neuroscience, Neurodegeneration and Repair, Yale University School of Medicine, New Haven, CT 06510 USA.
[6]Department of Cell Biology, Harvard Medical School, Boston, MA 02115, USA.
[7]Present address: Lee Kong Chian School of Medicine, Nanyang Technological University, 308232, Singapore.
*Correspondence: pietro.decamilli@yale.edu (P.D.C.)

THIS DOCUMENT INCLUDES:

Extended Experimental Procedures

Supplemental References

EXTENDED EXPERIMENTAL PROCEDURES

Cell Culture and Transfection

HeLa and COS-7 cells were cultured in Dulbecco's modified Eagle's medium (DMEM) containing 10% fetal bovine serum (FBS) and 1% penicillin/streptomycin at 37ºC and 5% CO2. Transfection of plasmids was carried out with Lipofectamine 2000 (Life Technologies). For siRNA experiments, HeLa cells were transfected with control or target siRNA oligos by using Lipofectamine RNAi MAX (Life Technologies) and cultured for 72 hours before analysis.

Generation of VAP Knockout Cell Lines with TALENs

TALEN construction and validation of targeted disruption of VAP genes

TALEN binding sites were chosen specific to exon 2 of VAPA and VAPB, respectively (**Figure 1A**). The VAPA and VAPB genomic sequences targeted by each pair of TALENs are: VAPA-TALEN-Left: 5'-TAGTCACTACAAATCTTAAA-3'; VAPA-TALEN-Right: 5'-TCACTTTGAAACACACTTTT-3'; VAPB-TALEN-Left: 5'-TTTTAAGGTGAAGACTACAG-3'; VAPB-TALEN-Right: TGATTCCGCTGTTGGGCCTC-3'. TALENs were constructed using the Golden-Gate ligation method as described (Miller et al., 2011; Sanjana et al., 2012). Assemblies of monomeric DNA-binding domains (designated by repeat variable diresidues, RVDs) and the TALEN cloning vectors used for each TALEN are:

VAPA-TALEN-Left: (NG) NI NN NG HD NI HD NG NI HD NI NI NI NG HD NG NG NI NI (NI), pTALEN_v2 (NI);

VAPA-TALEN-Right: (NG) HD NI HD NG NG NG NN NI NI NI HD NI HD NI HD NG NG NG (NG), pTALEN_v2 (NG);

VAPB-TALEN-Left: (NG) NG NG NG NI NI NN NN NG NN NI NI NN NI HD NG NI HD NI (NN), pTALEN_v2 (NN);

VAPB-TALEN-Right: (NG) NN NI NG NG HD HD NN HD NG NN NG NG NN NN NN HD HD NG (HD), pTALEN_v2 (HD).

HeLa cells were transiently transfected with plasmids expressing VAPA- and VAPB-specific TALENs respectively. After 72 hours, cells were harvested to extract genomic DNA. Regions surrounding the TALEN target sites of both loci were PCR amplified (with primers for VAPA: 5'_VAPA_DSB_400, GACACTGGTTTGCAGACAACTGG, 3'_VAPA_DSB_300, CACACTCCCTACACAGAAGATGAGTG; primers for VAPB: 5'_VAPB_DSB_345, GTGAGGTTTCAATGAGATGCCATATGTTAG, 3'_VAPB_DSB_255, GAAAAAAACAGGCGACTGGGACCCAGCTTTC). The PCR products were then melted and cross-hybridized such that wild type and TALEN-modified PCR products form homo- and heteroduplexes. Treatment with Surveyor Nuclease (Transgenomic) demonstrated TALEN cleavage efficiency of 11.5% for VAPA TALENs and 16.5% for VAPB TALENs (**Figure S1A**).

FACS enrichment of TALEN-modified cells

To enrich for gene-modified cells, a surrogate reporter system was used involving reporter plasmids that contain the TALEN target sequence framed between the coding sequences of mCherry and an out-of-frame EGFP (Kim et al., 2011) (**Figure S1B**). In this system mCherry is

constitutively expressed whereas EGFP is only expressed if the intervening TALEN target sequence is modified, so that expression of EGFP represents a proxy of TALEN-mediated gene modification of the endogenous sequence via the generation of double strand breaks followed by non-homologous end joining (NHEJ). To generate surrogate reporters for VAPA and VAPB, PCR amplicons containing the TALEN target sites were amplified (using the primers for VAPA: 5'_BglII_VAPA_Surro, GAGCTGTACAAGAGATCTGATGTAGTCACTACAAATCTTAAATTGCGAAATCCATCGTAC 3'_BamHI_VAPA_Surro, CGTCTCCTGGATCCATCACTTTGAAACACACTTTTGGTACGATGGATTTCGCAATTTAAG; and primers for VAPB: 5'_BglII_VAPA_Surro, GTACAAGAGATCTTGTTTTAAGGTGAAGACTACAGCACCACGTACGTACTGTGTGAGGCC, 3'_BamHI_VAPA_Surro, GTGGCGCCGGTGGATCCATGATTCCGCTGTTGGGCCTCACACAGTACGTACGTGGTGCTG) and ligated between BglII and BamHI in mCherry-E-Syt2-EGFP (Giordano et al., 2013) to generate mCherry-VAPA Surro-EGFP and mCherry-VAPB Surro-EGFP, respectively.

72 hours after transfection, cells co-expressing the TALEN pairs and the corresponding surrogate reporter were subjected to flow cytometry to enrich for cells double positive for mCherry and EGFP expression and thus likely to harbor TALEN-mediated VAP mutations.

Clonal isolation, verification of targeted gene disruption by DNA sequencing

Sorted cells were individually cloned. For either VAPA or VAPB TALENs, about 40 clones were analyzed by PCR genotyping of ~500 bp fragments surrounding the TALEN target sites, using one 6-carboxyfluorescein (6-FAM)-labeled primer and one regular primer. Names, sequences and 6-FAM label (if applicable) of these primers are:

5'_6FAM_VAPA_DSB_223, GACTTGTTTTTAAGTCTGCCACCTCG,

3'_VAPA_DSB_258, GCAGAGTACTGTAACAAGACATC,

5'_VAPB_DSB_243, CCTCAGCTCATCTCTTTCATCCATTGGC,

3'_6FAM_VAPB_DSB_179, TGGGGGTGGGGTGGAGAGAATTCTATCATCTTC.

Fragment analysis of the fluorescent PCR products with capillary electrophoresis (Genewiz) was then performed to resolve the length of the PCR amplicons of each clone. Clones carrying biallelic frameshift mutations were chosen. PCR amplicons of each such clone were ligated into pCR2.1 TOPO vectors using the TOPO-TA cloning kit (Life Technologies) and sequenced (Genewiz) for confirmation.

Three independent VAP double knockout (DKO) cell lines (DKO-1, -2, and -3) were generated. DKO-1 resulted from the single-round transfection of the VAPB-targeting TALENs which led to frameshift deletions in VAPB alleles. These TALEN pairs however, also resulted in the deletion of exon 2 in VAPA alleles due to an off-target-effect on its very similar, although not identical, sequence to exon 2 of VAPB (**Figure S1C**). Off-target effects of TALEN pairs at homologous sites are known to occur (Dahlem et al., 2012). DKO-2 and DKO-3 cell strains were generated by sequentially disrupting first the VAPA gene and then the VAPB gene. In both strains biallelic frameshift deletions on both VAPA and VAPB loci were detected.

Generation of Sac1 Knockout Cells with CRISPR/Cas9

The genomic sequence surrounding exon 5, which encodes the amino acid stretch at the beginning of the phosphatase domain of human Sac1, was analyzed for potential CRISPR/Cas9 targets *in silica* using the Cas9 design target tool (http://crispr.mit.edu) (Hsu et al., 2013). The Sac1 genomic sequence targeted by the predicted CRISPR gRNA with the highest "on-target score" is (with the PAM sequence underlined):

Sense strand: 5'-CCTTCCTAGCGATGCTAAACCAT-3',

Anti-sense strand: 5'-ATGGTTTAGCATCGCTAGGAAGG-3'.

The two sequences were synthesized and sub-cloned into a human codon-optimized Cas9 and chimeric gRNA expression plasmid that carries puromycin resistance, pSpCas9(BB)-2A-Puro (PX459), obtained from Addgene (Plasmid 48139) (Ran et al., 2013).

HeLa cells were transiently transfected with the Sac1 CRISPR/Cas9 plasmid. 24 hours after transfection, cells were supplemented with growth media containing puromycin (1.5 μg/mL) and incubated for 72 hours. Cells resistant to puromycin selection were then incubated with puromycin-free medium for 24 hours before harvesting for immunoblotting and imaging-based analysis.

DNA Plasmids

Sources of plasmids were as follows: M1 muscarinic acetylcholine receptor (M1R) (Bertil Hille, University of Washington, WA), EGFP-Rab7 (Bo van Deurs, University of Copenhagan), CH_{UTR}-mCherry (William Bement, University of Wisconsin-Madison), GFP-SNX9 (Kai Erdmann, University of Sheffield), GFP-GOLPH3 (Christopher Burd, Yale University), TGN46-GFP (Vas Ponnambalam, Leads University), GFP-CD-M6PR (Antonella De Matteis, Telethon Institute of Genetics and Medicine), VPS29-mCherry (Mark von Zastrow, University of California at San Francisco), YFP-FAM21 and YFP-WASH (Daniel Billadeau, Mayo Clinic), ST-mRFP (Jack Rohrer, University of Zurich), GFP-PH_{OSBP} (Tim Levine, UCL Institute of Ophthalmology), GFP-2xPH_{OSH2} (Tamas Balla, NIH), GFP-$P4C_{SidC}$ (Yuxin Mao, Cornell), Ruby-LifeAct (Roland Wedlich-Söldner, Max Planck Institute of Biochemistry), GFP-$PH_{PLC\sigma1,}$ iRFP-$PH_{PLC\sigma1}$, GFP-PIPK1γ-87, EGFP-Rab5, mRFP-Rab5, GFP-N-WASP, GFP-PI4KIIα, N-PH_{ORP5}-EGFP, N-PH_{ORP8L}-EGFP (our lab). The following plasmids were obtained from Addgene: GalT-EGFP (Plasmid 11929), mCh-Rab7A (Plasmid 61804), GFP-$P4M_{SidM}$ (Plasmid 51469).

To clone fluorescence-tagged VAP constructs, cDNA of VAPA and VAPB were PCR amplified from a total human brain cDNA library and sequence validated to correspond to the following GenBank entries: VAPA: NM_194434.2, VAPB: NM_004738.4. The following primers were used: EcoRI_VAPA_Fw, CAAGCTTCGAATTCGATGGCGTCCGCCTCAGGGGCCATGGCGAAG, BamHI_Stop_VAPA_Rv, GATCCGGTGGATCCCTACAAGATGAATTTCCCTAGAAAGAATCCAATG, EcoRI_VAPB_Fw, CAAGCTTCGAATTCGATGGCGAAGGTGGAGCAGGTCCTGAGCCTC, BamHI_Stop_VAPB_Rv, GATCCGGTGGATCCCTACAAGGCAATCTTCCCAATAATTACACCAAC. PCR products were ligated between EcoRI and BamHI for VAPA and VAPB in the pEGFP-C1 vector (Clontech) to generate EGFP-VAPA and EGFP-VAPB, and in the pmCherry-C1 (Clontech) to generate mCherry-VAPA and mCherry-VAPB. *P56S* mutation and *K87D M89D* double mutations in

VAPB were generated using a mutagenesis kit (QuikChange II XL, Agilent Technologies), with the following primers, respectively (targeted nucleotides are shown in lower case): VAPB_P56S_Fw, CAGCACCACGTAGGTACTGTGTGAGGtCCAACAGCGGAATCATCGATGCAGGGG, VAPB_P56S_Rv, CCCCTGCATCGATGATTCCGCTGTTGGaCCTCACACAGTACCTACGTGGTGCTG; VAPB_K87D-M89D_Fw, CCCAATGAGAAAAGTAAACACgacTTTgacGTTCAGTCTATGTTTGCTCC, VAPB_K87D-M89D_Rv, GGAGCAAACATAGACTGAACgtcAAAgtcGTGTTTACTTTTCTCATTGGG. The MSP domain construct was generated by PCR amplification from EGFP-VAPB using primers flanking the MSP domain of VAPB (KpnI_MSP-VAPB_Fw, GTCGACGGTACCGCGGTCCTGAGCCTCGAGCCGCAGCACG, BamHI_Stop_MSP-VAPB_Rv, CCGGTGGATCCCGGTCATTCAAACACACATCTAAG), and cloned into pEGFP-C1 vector between KpnI and BamHI.

GFP-PI4KIIβ was generated by PCR amplification from HA-PI4KIIβ (a kind gift from Tamas Balla) using the following primers: 5'_XhoI_PI4K2B, CTCAGATCTCGAGCTCATGGAGGATCCCTCCGAG, 3'_PstI_NonStop_PI4K2B, CCGTCGACTGCAGACCACCAGCACTCCAGGAGGAAAAAAATGGCTTCCTGC. PCR products were ligated between XhoI and PstI in the pEGFP-C1 vector (Clontech). To generate EGFP-SNX6, cDNA of SNX6 were PCR amplified from the total human brain cDNA library and sequence validated to correspond to the GenBank entry NM_152233.2, using the following primers: KpnI_SNX6_Fw, CGACGGTACCGCGGGCATGATGGAAGGCCTGGACGACG, BamHI_Stop_SNX6_Rv, CGGTGGATCCCGGTTATGTGTCTCCATTTAACACTGCC. PCR products were ligated between KpnI and BamHI in the pEGFP-C1 vector (Clontech). EGFP-SNX5 were generated by PCR amplified from cDNA clone of human SNX5 (Open Biosystems, clone ID: 7939468) using the following primers: KpnI_SNX5_Fw, CGACGGTACCGCGGGCATGGCCGCGGTTCCCGAGTTGCTGCAG, BamHI_SNX5_Rv, CCGGTGGATCCCGGTCAGTTATTCTTGAACAAGTCAATACAG). PCR products were ligated between KpnI and BamHI in the pEGFP-C1 vector (Clontech). OSBP-EGFP was generated by PCR amplified from cDNA clone of human OSBP (Open Biosystems, clone ID: 4560111) using the following primers: HindIII_OSBP_Fw, CTCGAGCTCAAGCTTATGGCGGCGACGGAGCTGAGAGGAGTGGTGGGGCCAG, BamHI_OSBP_Stop_Rv, CGACCGGTGGATCCCCGAAAATGTCCGGGCATGAGCTCCAGTCCTG. PCR products were ligated between HindIII and BamHI in the pEGFP-N1 vector (Clontech).

F18A, F28A and *F74A* mutations in SNX2 were generated using a mutagenesis kit (QuikChange II XL, Agilent Technologies), from wild type SNX2 as template with the following primers, respectively (targeted nucleotides are shown in lower case): SNX2_F18A_Fw, GCTGGGGGACGGGAAGCCCACCGACgcTGAGGATCTGGAGGACGGAGAGG, SNX2_F18A_Rv, CAGGTCCTCTCCGTCCTCCAGATCCTCAgcGTCGGTGGGCTTCCCGTCCCCC; SNX2_F28A_Fw, CTGGAGGACGGAGAGGACCTGgcCACCAGCACTGTCTCCACCCTAGAGTC, SNX2_F28A_Rv, CTTGACTCTAGGGTGGAGACAGTGCTGGTGgcCAGGTCCTCTCCGTCCTCC; SNX2_F74A_Fw, GATGATGACAGAGAAGATCTTgcTGCAGAAGCCACAGAAGAAGTTTC,

SNX2_F74A_Rv, CCAAAGAAACTTCTTCTGTGGCTTCTGCAgcAAGATCTTCTCTGTCATC). N-terminal alone truncation of SNX2 (YFP-SNX2$^{1-139}$) was generated by introducing a stop codon after the sequencing encoding the first 139 residues via mutagenesis, with the following primers (targeted nucleotides are shown in lower case): SNX2_NtermStop_Fw, GCAAATGGAGACATTTaaGACATAGAAATTGGTGTATCAGATCCAG, SNX2_NtermStop_Rv, CACCAATTTCTATGTCttAAATGTCTCCATTTGCTTCTTCTTCAATCTC). To generated iRFP-SNX2, cDNA of SNX2 was PCR amplified from YFP-SNX2, using the following primers: BspEI_SNX2_Fw, GAAGAGTCCGGAATGGCGGCCGAGAGGGAACCTCCTC, KpnI_Stop_SNX2_Rv, GATCCCGGGCCCGCGGTACCCTAGGCAATGGCTTTGGCTTCAGG. PCR products were ligated between BspEI and KpnI in the iRFP-FRB-Rab7 vector obtained from Addgene (Plasmid 51613).

siRNAs

Double-stranded siRNA were purchased from Integrated DNA Technologies with the following references: WASH (human WASH HSC.RNAI.N182905.12.1 from IDT), FAM21 (human FAM21 HSC.RNAI.N015262.12.2 from IDT), PI4KIIα (human PI4K2A HSC.RNAI.N018425.12.8), PI4KIIβ (human PI4K2B HSC.RNAI.N018323.12.1), OSBP (human OSBP HSC.RNAI.N002556.12.2 from IDT), SNX2 (HSC.RNAI.N003100.12.1 from IDT), Control (NC1 negative control duplex from IDT).

Antibodies and Chemicals

Antibodies obtained from the commercial sources include: rabbit polyclonal anti-VAPA (HPA009174, Sigma-Aldrich), anti-VAPB (HPA013144, Sigma-Aldrich), sheep polyclonal anti-TGN46 (AHP500GT, AbD Serotec), goat polyclonal anti-VPS35 (ab10099, Abcam), mouse monoclonal anti-EEA1 (clone 14, BD Tranduction Laboratories), mouse monoclonal anti-GM130 (clone 35/GM130, BD Tranduction Laboratories), rabbit polyclonal anti-p34 (07-227, EMD Millipore Corporation), mouse monoclonal anti-M6PR (IGF-IIR, clone 2G11, Santa Cruz), mouse monoclonal anti-clathrin heavy chain (clone TD1, American Type Culture Collection), mouse monoclonal anti-SNX2 (clone 13/SNX2, BD Transduction Laboratories), mouse monoclonal anti-c-Myc (clone 9E10, Santa Cruz), mouse monoclonal anti-GFP conjugated to HRP (Miltenyi Biotec), rat monoclonal anti-HA (clone 3F10, Roche), and mouse monoclonal anti-tubulin (clone B-5-1-2, Sigma-Aldrich). Alexa fluor phalloidin and Alexa fluor conjugated secondary antibodies were from Life Technologies. Rabbit polyclonal anti-PI4KIIα and anti-Sac1 antibodies were generated by our lab as previously described, respectively (Guo et al., 2003; Nemoto et al., 2000).

The following antibodies were kind gifts: rabbit anti-WASH and anti-FAM21 antibodies (Daniel Billadeau, Mayo Clinic), rabbit anti-PI4KIIβ (Helen Yin, UT Southwestern), rabbit anti-OSBP antibody (Hiroyuki Arai, University of Tokyo), rabbit anti-GRASP55, rabbit anti-Golgin97, mouse anti-P230, and rabbit anti-GRASP65 (James Rothman, Yale University),

Chemicals purchased from commercial sources include: puromycin, Oxo-M and Atropine (Sigma-Aldrich), Latrunculin B (Calbiochem), and PIK-93 (Selleckchem). VPS34 inhibitor VPS34-IN1 was obtained from Dr. Dario Alessi (University of Dundee). Compound A1 is a kind gift from Dr. Tamas Balla (NIH).

Fluorescence Microscopy

Fixed cells

Cells grown on glass coverslips (Neuvitro) were fixed with 4% PFA, washed in PBS, permeabilized with PBS containing 0.1% Saponin and 1% BSA, immunostained with designated antibodies in the same buffer and mounted using ProLong Gold anti-fade reagent (Invitrogen). Fixed cell samples were imaged by spinning disc confocal (SDC) microscopy. Images from a mid focal plane are shown.

Live cells

Cells were plated on 35 mm glass bottom dishes (MatTek Corp) at low density allowing attachment overnight, transfected and imaged with a SDC microscope 16-20 h after transfection. Before imaging, cells were transferred to imaging buffer containing 125 mM NaCl, 5 mM KCl, 1.3 mM $CaCl_2$, 1.2 mM $MgCl_2$, 25 mM HEPES, and 3 mM D-glucose with pH adjusted to 7.4 with NaOH.

Imaging

Spinning disc confocal (SDC) microscopy was performed using the Improvision UltraVIEW VoX system (Perkin-Elmer) built around a Nikon Ti-E inverted microscope and a Hamamatsu C9100-50 camera, equipped with PlanApo objectives (60 x 1.49-NA) and controlled by Volocity (Improvision) software. Total internal reflection fluorescence (TIRF) microscope was performed on a setup built around a Nikon TiE microscope equipped with 60 x 1.49-NA objectives. Excitation light was provided by 488-nm (for GFP and blue-light activation), 561-nm (mCherry and mRFP) and 640-nm (iRFP) DPSS lasers coupled to the TIRF illuminator through an optical fiber. The output from the lasers was controlled by an acousto-optic tunable filter and fluorescence was detected with an EM-CCD camera (Andor iXon DV-887). Acquisition was controlled by Andor iQ software.

Image Quantification

Fluorescence signal was quantified using Fiji (http://fiji.sc/wiki/index.php/Fiji). Data were processed with Excel (Microsoft) and plotted with Prism6 (GraphPad). Each dot represents value from a single cell with the black bar as the mean.

Colocalization analysis

Colocalization analysis was carried out by manually selecting an area of 15 x 15 μm^2, correcting background, and measuring the Pearson's correlation coefficient using the Fiji colocalization plug-in Coloc2.

Quantification of the endosomal localization of PI4P probes

Cells were co-transfected with a Golgi complex marker (ST-mRFP) and with PI4P probes that recognize with high affinity the Golgi and endosomal PI4P (GFP-$P4C_{SidC}$) (Luo et al. 2015). The fluorescence intensity of the mRFP channel, which produced the most intense signal in the Golgi complex area, was set to define the Golgi area of each cell. A region covering the entire cell, but excluding the Golgi complex area and the cell edge, was then manually selected (ROI) and the mean fluorescence pixel intensity in the ROI was calculated. Data is normalized by dividing the fluorescence intensity of the ROI of each cell by the average fluorescence intensity of the ROI of control cells.

Quantification of the plasma membrane localization of the PI4P probe via line scans

For this analysis, the N-PH_{ORP8L}-GFP probe was used. This is a low affinity "sensor" of plasma membrane PI4P that remains primarily in the cytosol and even more in the nucleus under control conditions, but relocates to the plasma membrane in response to the increase of PI4P in this membrane (Chung et al., 2015). A line of 5 µm in length was manually drawn perpendicular to the plasma membrane (see dashed lines in **Figure 2F**, **2L**). Fluorescence pixel intensity along the line was calculated and normalized by dividing the fluorescence of each pixel by the average fluorescence intensity of the line in the cytosolic region.

Quantification of WASH and actin on endosomes

Cells were immunostained for WASH and EEA1 and stained with fluorescent phalloidin. Images were background corrected, and EEA1 fluorescence was used to define the area (ROI) occupied by early endosomal compartments. The fluorescence intensity of WASH immunoreactivity and of phalloidin within the ROI was then measured (see examples in the right fields in **Figure S7G**, **S7H**, and **S7I**). Data were normalized by dividing the fluorescence intensity value of each pixel by the average fluorescence intensity observed in the ROI of control cells.

Quantification of the traffic of internalized antibody directed against CI-MPR

Cells were incubated at 37ºC in serum-free DMEM containing 10 µg/mL mouse anti-CI-MPR mAb for up to 60 min, quickly rinsed with PBS, and then stained for the internalized antibodies by immunofluorescence as described above. Images were background corrected, and the total intracellular (internalized) fluorescence intensity was measured by manually selecting an area covering the entire cell. The fluorescence intensity within a 10 x 10 μm^2 region centered on the Golgi complex was then measured (see dashed boxes in **Figure 2H**). The non-Golgi fluorescence intensity was obtained by subtracting the fluorescence intensity in the Golgi complex from the total fluorescence intensity. Data was presented as the non-Golgi/Golgi CI-MPR fluorescence ratio from each cell.

Phosphoinositide Analysis

WT and VAP DKO cells at 60% confluency on 10 cm dishes were metabolically labeled with [^{3}H]myo-inositol (MP Biomedicals) in inositol-free DMEM (MP Biomedicals) for 48 h. Lipid extraction and HPLC analysis was performed as described previously (Nakatsu 2012; Chung 2015b). Briefly, cells were washed twice with PBS, lysed with 4.5% perchloric acid, collected by scraping and centrifuged into pellets. The pellets were rinsed with ice-cold 0.1 M EDTA, deacylated with a mixture of methylamine/water/*n*-butanol/methanol (36:8:9:47) for 1 h at 50ºC and dried in a SpeedVac (Savant). The residue was extracted using a mixture of *n*-butanol/petroleum ether/ethyl formate (20:40:1) and water. Deacylated phosphoinositides were then separated using high performance liquid chromatography (Shimadzu Scientific Instruments) and detected by an online flow scintillation analyzer (B-RAM, IN/US).

Immunoblotting

HeLa cells were lysed in buffer containing 2% SDS, 150 mM NaCl, 10 mM Tris (pH 8.0), and incubated at 60ºC for 20 min followed by incubation at 70ºC for 10 min. The lysates were treated with Benzonase Nuclease (Novagen) for 30 min at room temperature. Cell lysates were

processed for SDS-PAGE and immunoblotting with standard procedure. All immunoblotting were developed by chemiluminescence using the SuperSignal West Dura reagents (Thermo Fisher Scientific).

Immunoprecipitation

HeLa cells expressing the indicated constructs were washed in cold PBS and lysed on ice in lysis buffer [50 mM Tris, 150 mM NaCl, 1% digitonin, 0.5 mM EDTA, 10% glycerol, pH 7.4 and protease inhibitor cocktail (Roche)]. Cell lysates were then centrifuged at 21,000 g for 20 min at 4ºC. For anti-GFP immunoprecipitation, supernatants were incubated with Chromotek GFP-trap agarose beads (Allele Biotech) for 2 h at 4ºC under rotation. Subsequently, beads were washed in lysis buffer containing 1% digitonin once and 0.2% digitonin twice. Afterwards, immunoprecipitated proteins bound to the beads were incubated in PAGE sample loading buffer (containing 2% SDS) and then incubated at 60ºC for 20 min and 70ºC for 10 min. Immunoprecipitates were processed for SDS-PAGE and immunoblottings were carried out as described above.

Mass spectrometry analysis of VAP and SNX2 interactions

Plasmids

ORF clones of VAPB WT, VAPB FFAT, and SNX2 were sequentially cloned into the pDONR223 entry vector and the lentiviral destination vectors pHAGE-N-FLAG-HA-PURO and pHAGE-N-GFP-BLAST using λ-recombinase (Gateway system).

Cell culture and generation of stable cell lines

HEK293T and HeLa cells (ATCC) were cultured in DMEM supplemented with 10% Fetal Bovine Serum (FBS) (Hyclone) at 37°C/5% CO_2. Plasmid DNA and viral helper constructs (VSVG, TAT1B, MGPM2, CMV-Rev1B) at a 4:1 ratio (transgene:helper) were diluted in OptiMEM (Gibco), and combined with 1µg/µl polyethylenimine (PEI) (Polysciences Inc.) in a 3:1 ratio (PEI:total DNA). The PEI/DNA mix was added to HEK293T cells followed by incubation at 37°C/5% CO_2 for 16 hours. The DMEM media was refreshed and cells were incubated for an additional 24 hours for virus production. Viral supernatant collected from these cells supplemented with 1µl polybrene (8mg/mL) was used to infect HeLa cells. Stable HeLa cell lines were generated 48-72 hours post infection through the addition of selection media containing puromycin (1µg/mL) and blasticidin (10µg/mL).

Immunoprecipitation and CompPASS proteomic analysis

AP-MS and CompPASS analysis (using the Comparative Proteomics Analysis Software Suite) were performed as previously described (Sowa et al., 2009). For each immunoprecipitation, stable cell lines from 4x15cm dishes at 80% confluence were harvested in lysis buffer (50 mM Tris-HCl/pH 7.5, 150mM NaCl, 1 mM EDTA, 1 mM EGTA, 50 mM sodium fluoride, 5 mM sodium pyrophosphate, 10 mM sodium glycerol 2-phosphate, 1mM sodium orthovanadate, 0.27M sucrose, 1% (v/v) NP-40, 1 mM DTT) supplemented with protease inhibitors (Roche) to produce whole cell extracts. Whole cell extracts were sonicated, clarified by centrifugation (16000xg for 10 minutes/4°C), and filtered through 0.45m filters (Sartorius). Immunoprecipitation was performed with 60µL/50% slurry anti-HA agarose resin (SIGMA) for 4 hours at 4°C. Beads were washed with lysis buffer (3x) and with phosphate buffered saline/pH

7.2 (PBS) (2x). The immunoprecipitated bait was eluted twice (30 minutes at 30°C each) with HA peptide (250 μg/ml) (Bio-Synthesis Inc) diluted in PBS. Eluates were reductively carboxymethylated and precipitated using 20% trichloroacetic acid (TCA).

TCA-precipitated proteins were resuspended in 200mM HEPES buffer with 200ng of sequencing grade trypsin (Promega) and incubated overnight at 37°C. Digestion was quenched with 5% formic acid (FA)/5% acetonitrile (ACN) and de-salted using C18 stage tips. Peptides were eluted with 5% FA/75% ACN, dried using a speedvac, and resuspended in 5% FA/5% CAN. Samples were processed in technical duplicate on an LTQ Velos (Thermo) mass spectrometer, and spectra search with Sequest prior to target-decoy peptide filtering, and linear discriminant analysis. Protein Assembler was used to convert spectral counts to average protein spectral matches (APSMs), which takes into account peptides that match more than one protein in the database. Peptides were identified with a false discovery rate of < 1.0%. The following MS2 conditions were used: Activation Type – Collision induced dissociation; Minimum Signal Required - 2000.0; Isolation width (m/z) - 1.00; Normalized Collision Energy - 35.0; Default Charge State – 2; Activation Q - 0.250; Activation Time (ms) - 10.000. Peptide data (APSM) were uploaded into the CompPASS algorithm. The CompPASS system identifies high confidence candidate interacting proteins (HCIPs) based on the normalized weighted D (NWD)-score, which incorporates the frequency with which they identified within the stats table, the abundance (APSMs, average peptide spectral matches) when found, and the reproducibility of identification in technical replicates, and also determines a z-score based on APSMs (Sowa et al., 2009).

Immunoprecipitation and quantitative/TMT proteomic analysis

For quantitative proteomic analyses, AP-MS was performed using three independent biological replicate samples. Stable HeLa cell lines were harvested as described in the previous section. Each immunoprecipitation was performed using 60μL/50% slurry anti-FLAG magnetic beads (SIGMA) for 4 hours at 4°C. Beads were washed with lysis buffer (3x) and with elution buffer (50mM Tris/pH 8.0, 150mM NaCl) (2x). The immunoprecipitated bait was eluted twice (10 minutes at 25°C each) with 3xFLAG peptide (250 μg/ml) diluted in elution buffer. Eluates were precipitated and digested as previously described. Peptides derived from the various samples (triplicate independent immunoprecipitation per bait) were subjected to 6-plex TMT analysis using an Orbitrap Fusion mass spectrometer (Thermo Fisher Scientific, San Jose, CA) coupled to a Proxeon EASY-nLC II liquid chromatography (LC) pump (Thermo Fisher Scientific), using multinotch MS3 (McAlister et al., 2014; Ting et al., 2011) with synchronous-precursor-selection (SPS) where precursor ions (n=10) were collected. For quantification, a 0.03 *m/z* window centered on the theoretical *m/z* value of each of six reporter ions and the closest signal intensity from the theoretical *m/z* value was recorded. Total signal to noise values for all peptides were summed for each TMT channel, and all values were adjusted to account for variance in sample handling. The peptide intensities were normalized to the bait. For each peptide, a total minimum signal to noise value of 100 was required.

SUPPLEMENTAL REFERENCES

Chung, J., Torta, F., Masai, K., Lucast, L., Czapla, H., Tanner, L.B., Narayanaswamy, P., Wenk, M.R., Nakatsu, F., and De Camilli, P. (2015). INTRACELLULAR TRANSPORT. PI4P/phosphatidylserine countertransport at ORP5- and ORP8-mediated ER-plasma membrane contacts. Science *349*, 428–432.

Dahlem, T.J., Hoshijima, K., Jurynec, M.J., Gunther, D., Starker, C.G., Locke, A.S., Weis, A.M., Voytas, D.F., and Grunwald, D.J. (2012). Simple methods for generating and detecting locus-specific mutations induced with TALENs in the zebrafish genome. PLoS Genet. *8*, e1002861.

Giordano, F., Saheki, Y., Idevall-Hagren, O., Colombo, S.F., Pirruccello, M., Milosevic, I., Gracheva, E.O., Bagriantsev, S.N., Borgese, N., and De Camilli, P. (2013). PI(4,5)P(2)-dependent and Ca(2+)-regulated ER-PM interactions mediated by the extended synaptotagmins. Cell *153*, 1494–1509.

Guo, J., Wenk, M.R., Pellegrini, L., Onofri, F., Benfenati, F., and De Camilli, P. (2003). Phosphatidylinositol 4-kinase type II alpha is responsible for the phosphatidylinositol 4-kinase activity associated with synaptic vesicles. Proc. Natl. Acad. Sci. U.S.a. *100*, 3995–4000.

Hsu, P.D., Scott, D.A., Weinstein, J.A., Ran, F.A., Konermann, S., Agarwala, V., Li, Y., Fine, E.J., Wu, X., Shalem, O., et al. (2013). DNA targeting specificity of RNA-guided Cas9 nucleases. Nat. Biotechnol. *31*, 827–832.

Kim, H., Um, E., Cho, S.-R., Jung, C., Kim, H., and Kim, J.-S. (2011). Surrogate reporters for enrichment of cells with nuclease-induced mutations. Nat. Methods *8*, 941–943.

Luo, X., Wasilko, D.J., Liu, Y., Sun, J., Wu, X., Luo, Z.-Q., and Mao, Y. (2015). Structure of the Legionella Virulence Factor, SidC Reveals a Unique PI(4)P-Specific Binding Domain Essential for Its Targeting to the Bacterial Phagosome. PLoS Pathog. *11*, e1004965.

Miller, J.C., Tan, S., Qiao, G., Barlow, K.A., Wang, J., Xia, D.F., Meng, X., Paschon, D.E., Leung, E., Hinkley, S.J., et al. (2011). A TALE nuclease architecture for efficient genome editing. *29*, 143–148.

Nemoto, Y., Kearns, B.G., Wenk, M.R., Chen, H., Mori, K., Alb, J.G., De Camilli, P., and Bankaitis, V.A. (2000). Functional characterization of a mammalian Sac1 and mutants exhibiting substrate-specific defects in phosphoinositide phosphatase activity. J. Biol. Chem. *275*, 34293–34305.

Ran, F.A., Hsu, P.D., Wright, J., Agarwala, V., Scott, D.A., and Zhang, F. (2013). Genome engineering using the CRISPR-Cas9 system. Nat Protoc *8*, 2281–2308.

Roy, A., and Levine, T.P. (2004). Multiple pools of phosphatidylinositol 4-phosphate detected using the pleckstrin homology domain of Osh2p. J. Biol. Chem. *279*, 44683–44689.

Sanjana, N.E., Cong, L., Zhou, Y., Cunniff, M.M., Feng, G., and Zhang, F. (2012). A transcription activator-like effector toolbox for genome engineering. Nat Protoc *7*, 171–192.

Sowa, M.E., Bennett, E.J., Gygi, S.P., and Harper, J.W. (2009). Defining the human deubiquitinating enzyme interaction landscape. Cell *138*, 389–403.